

# Multifunctional Ferrofluid-Infused Structured Surfaces

## with Dynamically Reconfigurable Multiscale Topography

Wendong Wang<sup>†1,2,3</sup>, Jaakko V. I. Timonen<sup>†1,4</sup>, Andreas Carlson<sup>1,2,5</sup>, Dirk Drotlef<sup>3</sup>, Cathy T.Y. Zhang<sup>1,2</sup>, Stefan Kolle<sup>1</sup>, Alison Grinthal<sup>1</sup>, Tak-Sing Wong<sup>1,2</sup>, Benjamin Hatton<sup>1,2</sup>, Sung Hoon Kang<sup>1,2</sup>, Stephen Kennedy<sup>1,2</sup>, Joshua Chi<sup>1,6</sup>, Robert Thomas Blough<sup>2</sup>, Metin Sitti<sup>3</sup>, L. Mahadevan<sup>1,2,7</sup>, Joanna Aizenberg<sup>1,2,6,7\*</sup>

<sup>1</sup>John A. Paulson School of Engineering and Applied Sciences, Harvard University, Cambridge, Massachusetts 02138, USA. <sup>2</sup>Wyss Institute for Biologically Inspired Engineering, Harvard University, Cambridge, Massachusetts 02138, USA. <sup>3</sup>Max Planck Institute for Intelligent Systems, Stuttgart, 70569, Germany. <sup>4</sup>Department of Applied Physics, Aalto University School of Science, Espoo FI-02150, Finland. <sup>5</sup>Department of Mathematics, Mechanics Division, University of Oslo, 0851 Oslo, Norway. <sup>6</sup>Department of Chemistry and Chemical Biology, Harvard University, Cambridge, Massachusetts 02138, USA. <sup>7</sup>Kavli Institute for Bionano Science & Technology, Harvard University, Cambridge, Massachusetts 02138, USA.

**Developing adaptive material systems whose geometries change in response to external stimuli not only generates fundamental insights into the relationship between the shape-altering physical forces and the resulting morphologies, but also has immense technological relevance in areas from creating dynamic interfaces with biological tissues to designing energy-efficient aircrafts<sup>1,2</sup>. In particular, reconfigurable surface topography has been designed using responsive gels<sup>3</sup>, shape-memory polymers<sup>4</sup>, liquid crystals<sup>5-7</sup>, or hybrid composites<sup>8-13</sup> through biomimetic approaches to control interfacial properties<sup>14</sup>. The resulting functions of these existing designs are restricted by the limited types of their structure-specific topographical changes. Here we show a hierarchical magneto-responsive composite surface made by infiltrating an active component—ferrofluid—into a passive microstructured matrix (so-called ferrofluid-containing liquid-infused porous surfaces—FLIPS), and demonstrate unique topographical reconfigurations at multiple length scales and a broad range of associated emergent behaviours. The magnetic field induces the movement of nanoscopic magnetic nanoparticles, which leads to microscopic flow of ferrofluid first above and then within the microstructured surface. This redistribution changes the initially smooth surface of the ferrofluid immobilized by the porous matrix through capillary force, into various multiscale hierarchical topographies shaped by the size, arrangement and orientation of the confining microstructures in the magnetic field. We provide detailed theoretical and experimental analyses of the spatial and temporal dynamics of these reconfigurations based on the balance between capillary and magnetic pressure<sup>15-19</sup> and geometrical anisotropy of the FLIPS system. A number of interesting functions at three different length scales are demonstrated: at micron-scale, manipulation and self-assembly of colloidal particles; at millimeter scale, flow control of liquid droplets; at centimeter scale, switchable adhesion and friction, liquid pumping, and removal of biofilms. We envision that FLIPS can be developed into an integrated platform for exploring and designing control systems for manipulation and transport of matter, thermal management, microfluidics, and fouling-release materials.**

While the magnetic field-induced reconfiguration of a ferrofluid to form macroscopic protuberances on a flat surface is well known<sup>15,16</sup>, we anticipated that ferrofluid’s behaviour in the microstructured confinement may elicit a range of otherwise unachievable multiscale topographical responses enabled by the capillary pressure within the porous substrate (**Fig. 1a**). To explore this concept, we used a variety of microstructured substrates (see Table 1) infiltrated with fluorocarbon- or silicone oil-based ferrofluid. The spatiotemporal changes in surface topography occurring upon application of a magnetic field were visualized using an angled illumination technique, the thickness of the ferrofluid overlayer was measured using a force probe (see **Extended Data Fig. 1**) and the evolution of the profile of the ferrofluid-air interface was measured using a laser scanning microscope (**Extended Data Fig. 2a,b**).

Table 1. Structured surfaces used in this study

Pattern #	Pattern type	Dimensions ( $\mu\text{m}$ )
1	Array of microchannels	$dx=0; dy=38; h_0=34$
2	Array of microchannels	$dx=0; dy=38; h_0=15$
3	Array of microchannels	$dx=0; dy=76; h_0=34$
4	Array of microplates	$dx=5; dy=38; h_0=30$
5	Array of microposts	$dx=1.4; dy=1.4; h_0=10$
6	Spirally-shaped channels	$dx=0; dy=38; h_0=15$
7	Microporous membrane	Average pore size = 1
8	Microporous membrane	Average pore size = 10
9	Microporous membrane	Average pore size = 20
10	Microporous tubing	Average pore size = 5-60

The non-uniform magnetic field created by a magnet below FLIPS initiates three sequential and interrelated processes to generate dynamic multiscale topographies (**Fig. 1b**). In the first step, the magnet starts to withdraw the initially flat ferrofluid overlayer. Withdrawal leads to the formation of a macroscopic protuberance with lateral size comparable to that of the magnet (ca. 1 - 20 mm). In the second step, the ferrofluid that remains trapped in the porous matrix through capillary force is pulled out of the pores by a magnetic pressure  $|p_m| \approx \mu_0 M_s H_0$  (**Extended Data Fig. 3a-c**), where  $\mu_0$  [ $\text{N}\cdot\text{A}^{-2}$ ] is the vacuum permeability,  $M_s$  [ $\text{A}\cdot\text{m}^{-1}$ ] the saturation magnetization of the ferrofluid, and  $H_0$  [ $\text{A}\cdot\text{m}^{-1}$ ] the strength of the applied magnetic field<sup>15</sup>. The magnetic pressure is counteracted by the capillary pressure  $p_\gamma \approx 2\gamma/dy$ , where  $\gamma$  is the surface tension of the ferrofluid-air interface and  $dy/2$  is half of the width of the channels and the largest characteristic radius of the porous matrix. If  $|p_m| \leq p_\gamma$ , ferrofluid will remain trapped in the pores (**Extended Data Fig. 3e-g**). If  $|p_m| > p_\gamma$ , such as the case shown in **Fig. 1b** and **Extended Data Fig. 3d**, where  $|p_m| \approx 10^4$  Pa and  $p_\gamma \approx 10^3$  Pa, ferrofluid will be extracted from the pores, leading to the appearance of the conformally-coated micro-topographic region *I*. In the third step, the micro-topographical area expands outwards through porous-capillary flow, while the macroscopic protuberance continues to grow through the accumulation of ferrofluid. The initial extraction of ferrofluid from the areas around the magnet deforms the ferrofluid-air interface. This interface deformation induces a capillary force along the microstructures, even in areas far from the magnet where the magnetic pressure is smaller than capillary pressure. Over time, the interface has a gradually increasing height along the channel, from its minimum near the magnet to its maximum height  $h_0$  in the far field (**Fig. 1c** and **Extended Data Fig. 2b**). The combination of the magnetic suction force and the capillary force makes the flow follow the micro-topography, even in highly complex channel geometries such as a spiral shape of pattern #6, where the flow makes turns along a curved path (see **Extended Data Fig. 2e**).

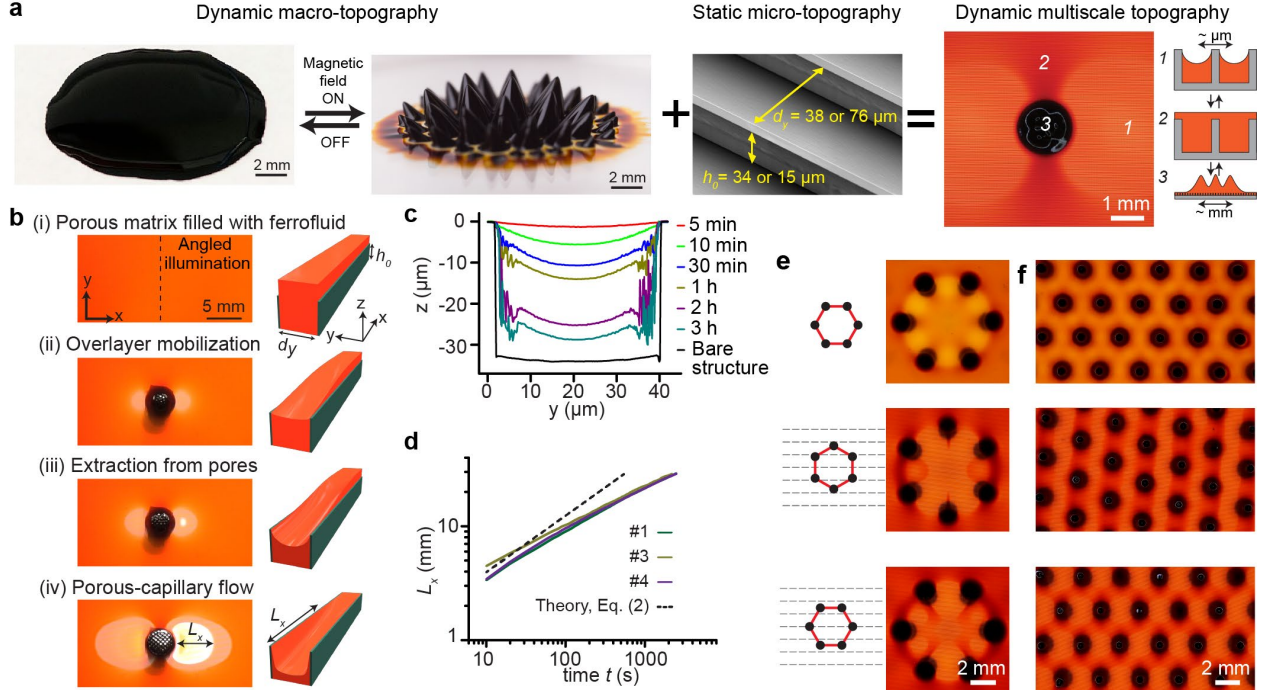


**Figure 1. Dynamic multiscale topography of ferrofluid-containing liquid-infused porous surface (FLIPS).** (a) A diagram showing the concept of FLIPS. Left: Two topographic states of a ferrofluid spreading on an unstructured surface, depicting the transformation from the flat interface to macroscopic protuberances in response to an external magnetic field. Middle: Scanning electron micrograph (SEM) of the static micro-topography of exemplary microchannel substrates #1-3 (see **Table 1**). Right: Top view photo of FLIPS under magnetic field, showing that the ferrofluid confined within the microstructured solid experiences unique, area-selective topographical reconfigurations at multiple length scales: region 1 exhibits micro-topography shaped by the structured substrate; region 2 exhibits a flat surface, and region 3 exhibits the macro-topographical protuberance. (b) Transport processes involved in the formation of macro- and micro-topographical features: the left column shows a series of representative experimental photos in top view captured using the angled illumination technique (see **Extended Data Fig. 1b**); the right column shows the corresponding schematics depicting the deformation of the ferrofluid-air interface in a microchannel. (c) Evolution of cross-section profiles of ferrofluid-air interface at a fixed distance ( $\sim 1.5$  cm away from the magnet) over time measured using a laser scanning microscope. (d) The log-log plots of experimentally measured  $L_x$  versus time  $t$  for surfaces #1, 3, 4 from **Table 1**. The dashed black line is plotted according to equation (2), with  $\gamma = 17$  mN/m,  $\eta = 0.367$  Pa.s and  $h_0 = 34$   $\mu\text{m}$ . See **Supplementary Video 1** for a representative movie showing the spatiotemporal evolution of the multiscale topography. The overlayer thicknesses are  $\sim 10$ – $20$   $\mu\text{m}$ . (e-f) Multiscale topographical response to a hexagonal pattern of six (e) or more (f) magnets (diameter 1.6 mm, magnet spacing 3.2 mm): the top row shows the case without the microstructured substrate; the bottom two rows show the cases with the microstructured substrate #4 but different orientation of the hexagonal pattern. See **Supplementary Video 1**.

The size of the micro-topographical area, characterized by  $L_x$ , was observed to scale with time as  $L_x \sim t^{0.35-0.5}$  for different patterns and overlayer dimensions tested (**Fig. 1d** and **Extended Data Fig. 2c,d**). By balancing the rate of change of work done by the capillary force with the viscous dissipation, we obtain

$$(\gamma L_x \dot{d}_y) \approx \gamma d_y U \approx \int \eta \left( \frac{\partial U}{\partial z} \right)^2 dV \approx \eta \left( \frac{U}{h_0} \right)^2 h_0 L_x d_y, \quad (1)$$

Where  $U \approx \dot{L}_x$  and  $\dot{L}_x = dL_x/dt$ . Rearranging the terms and integrating with respect to time  $t$  gives a scaling relation for  $L_x$  that correlates well with the experimental data:

$$L_x(t) \approx \left( \frac{\gamma h_0}{\eta} \right)^{1/2} \cdot t^{1/2}, \quad (2)$$

where  $\gamma$  is the surface tension;  $\eta$  is the dynamic viscosity;  $h_0$  is the height of the microstructure. The magnetic pressure  $|p_m|$  generates a force on the ferrofluid, where an alternative derivation to the scaling relationship (2) is obtained by replacing the left hand side of (1) by the rate of change of work done by the magnet on the ferrofluid ( $|p_m| \dot{L}_x d_y h_0$ ) and integrating with respect to time:

$$L_x(t) \approx \left( \frac{|p_m| h_0^2}{\eta} \right)^{1/2} \cdot t^{1/2}. \quad (3)$$

Both derivations give the same power law dependence with respect to time  $L_x \sim t^{1/2}$  and only differ in pre-factors. Despite their simplicity, these scaling relations provide a reasonable order-of-magnitude approximation to describe the dynamics revealed in the experimental data. They also capture the dependence of  $L_x$  on  $h_0$  and the independence of  $L_x$  from  $d_x$  and  $d_y$ . The discrepancy between the experiments and these scaling laws may be due to the three-dimensional shape of the microchannels, the complex shape of the ferrofluid-air interface and the dependence on the thickness of the ferrofluid overlayer (see **Extended Data Fig. 2c**) that the current models do not fully capture.

The asymmetry of the microchannels used in the demonstrations above induces preferential asymmetric extraction of the ferrofluid from the channels along the x-direction and the appearance of the characteristic dumbbell-shaped micro-topographical signature (**Supplementary Video 1**). Additional length scales can be introduced by using patterned or structured magnetic fields applied to geometrically anisotropic FLIPS. Such fields can be created by organizing multiple permanent magnets into an array. For example, a hexagonal cluster of six magnets acting on a FLIPS with a channel-like array of microplates introduces one more symmetry element to the system, leading to more complicated flow patterns that reflect the relative orientation of the anisotropic microstructures in the patterned magnetic field (**Fig. 1e**). Since the field source is no longer axisymmetric, the orientation of the field source (6-fold rotational symmetry) with respect to the microplates (2-fold rotational symmetry) allows for one more degree of control over the topographical response (**Fig. 1e** and **Supplementary Video 1**), with the opportunities to be expanded to any combination of the magnet assembly (e.g., “infinite” arrays of magnets, see **Fig. 1f**) and the structured surface.

The FLIPS concept introduced here offers unprecedented versatility and modularity in designing dynamic surfaces with multiscale topographical responses. In the examples shown above and below, we demonstrate that the specific topographical patterns can be finely tuned by controlling (i) the properties of the ferrofluid (e.g. concentration and type of magnetic particles or the type and viscosity of the carrier fluid); (ii) the geometry of the microstructured substrate; (iii) the strength and the pattern of the magnetic field; and (iv) the relative orientation and distance of the FLIPS from the magnets. The resulting spatial and temporal dynamics of topographical reconfiguration enable numerous functions at multiple length scales.

At the micron scale, FLIPS offers a new approach for manipulation of colloidal matter on 2D interfaces (**Fig. 2**). Depending on the state of the dynamic topography, colloidal particles can form a disordered 2D gas-like state (on flat topography, **Fig. 2a**) or organize into structures such as chains (on micro-topographic regions, **Fig. 2b**). Subsequently, FLIPS allows for controlled

transport of non-magnetic colloids when a horizontal body force on the ferrofluid is exerted by a lateral magnetic field gradient (**Fig. 2c,d**). The transport mechanism is unique, as it does not correspond to either positive or negative magnetophoresis of magnetic colloidal matter that have been studied extensively before<sup>20</sup>. Instead, the force on the non-magnetic particle is created hydrodynamically by coupling of the ferrofluid flow under the field gradient to the motion of the aqueous phase on top of the ferrofluid (**Fig. 2e**). Under typical experimental conditions utilizing small permanent magnets as field sources, the speed of the colloids is on the order of a few  $\mu\text{m/s}$  and controllable with the magnetic field (**Fig. 2f and Supplementary Video 2**).

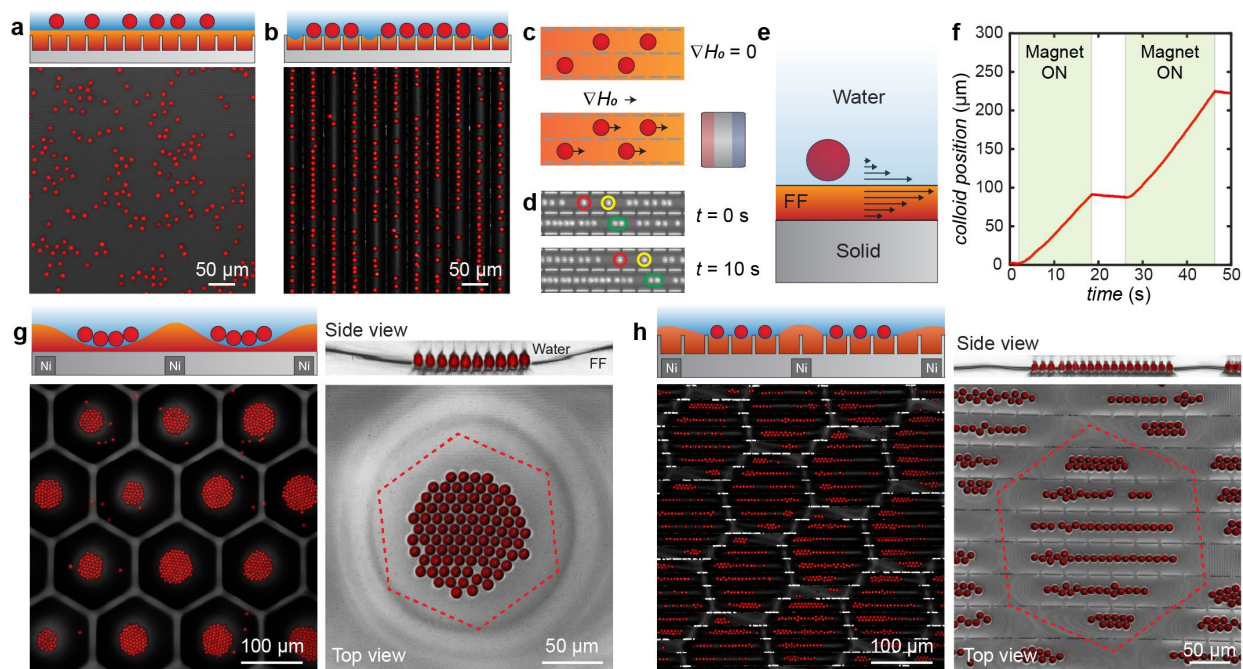


**Figure 2. Applications of FLIPS at the micron scale: manipulation of non-magnetic colloidal particles on FLIPS.** (a-b) Schematic and confocal fluorescence images of 10  $\mu\text{m}$  melamine colloidal particles floating on the flat surface of FLIPS in the absence of a magnetic field (a) and confined in micro-topography of FLIPS when ferrofluid has been locally depleted from the microstructures with a magnet (b). (c) Schematics showing colloidal particles staying stationary in the absence of a magnetic field gradient (top) and moving in the presence of a magnetic field gradient (bottom). (d) Optical images showing the transport of colloidal particles along the micro-topographical region. Four particles are labelled to depict their movement within a 10s interval. See **Supplementary Video 2**. (e) Schematic illustrating the mechanism behind the transport of non-magnetic colloidal particles in a magnetic field: the transport of ferrofluid induces a flow of water near the ferrofluid-water interface, and this induced water flow moves the colloidal particles. (f) Plot of colloidal position vs. time. (g-h) Schematic and confocal fluorescence images showing the confinement of colloidal particles by the macro-topographical response of a thin layer of ferrofluid alone (without micro-topography) (g) and the confinement of colloidal particles by the macro- and micro-topographical response of FLIPS (h). A hexagonal nickel grid embedded in FLIPS is used to shape a nearly uniform external magnetic field into a hexagonally varying field intensity pattern.

Multiscale topography can also be used for assembling colloidal matter into otherwise inaccessible hierarchical structures. For example, in the case of ferrofluid alone, a hexagonal soft ferromagnetic nickel grid leads to the formation of a hexagonally varying periodic ferrofluid pattern on which colloidal particles assemble into close-packed clusters (**Fig. 2g**), whereas in the

case of FLIPS, a multiscale topographical response is created, and colloidal matter organizes into short line segments as dictated by the two symmetries (**Fig. 2h**).

At the millimeter scale, FLIPS can be harnessed for controlling the motion, clustering, and interaction of liquid droplets. We use gravitational force to drive the flow of droplets on a tilted FLIPS, and tune the multiscale topographical response by adjusting the magnetic field strength and gradients through varying the distance,  $d$ , between the magnet and FLIPS (**Fig. 3a**). On one hand, the reversible appearance of micro-topography creates switchable slippery surfaces<sup>21</sup> that pin the droplets at micro-topographical regions or release the droplets when the magnetic field strength is reduced to remove the micro-topography (**Fig. 3b**, **Supplementary Video 3**). On the other hand, the macro-topographical protuberance can be used for assembling droplets into well-defined clusters (**Fig. 3c**). To demonstrate this unique behavior, we note that when a droplet slides near the protuberance, it is pinned to it by capillary and magnetic forces. Subsequent droplets will enter the trap and combine with the previously pinned droplets to form clusters, until their collective gravity overcomes their attraction to the protuberance. Then they are released as doublets, triplets, quadruplets, or quintuplets, depending on the adhesion controlled by the distance between the magnet and the FLIPS (**Supplementary Video 4**). If the droplets contain polymerizable moieties, these clusters can be solidified into distinct assemblies.

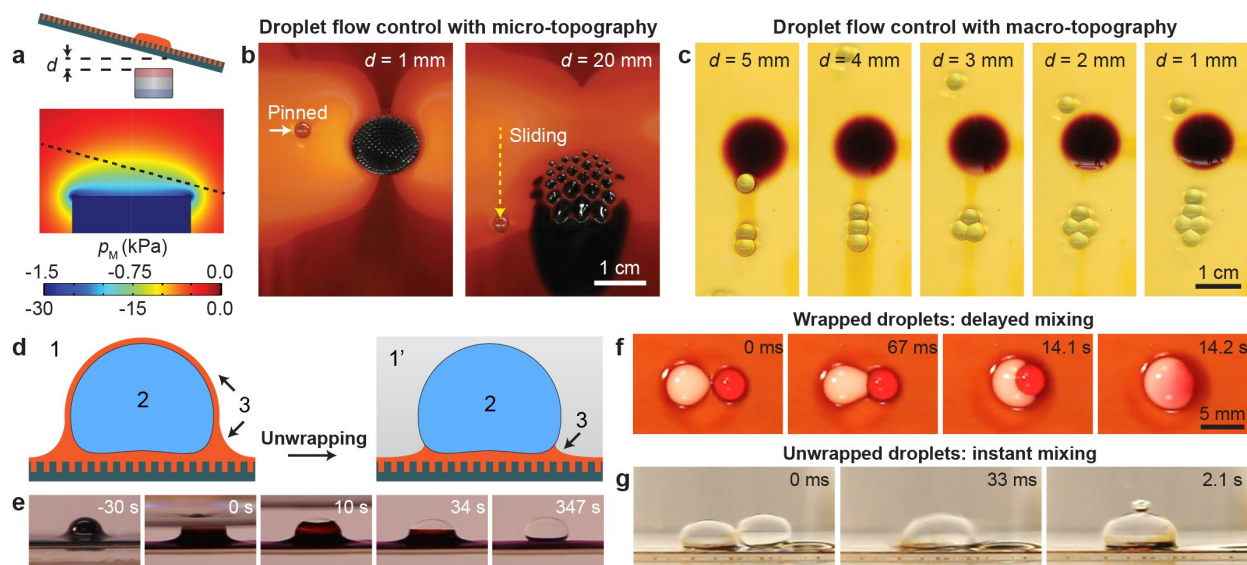


**Figure 3. Applications of FLIPS at the millimeter scale: droplet flow control and droplet manipulation.** (a) Top: Schematic showing the configuration of experimental set-up in (b) and (c). FLIPS is tilted and placed above the magnet. The distance  $d$  between the magnet and FLIPS can be varied. Bottom: Simulated graph of the magnetic pressure distribution around the magnet. The upper and lower scales of the legend for the magnetic pressure distribution correspond to (c) and (b), respectively. (b) Two photographs showing a water droplet pinned on the micro-topographical area and its subsequent release after the magnet was lowered to allow ferrofluid to flow back and submerge the micro-topography. See **Supplementary Video 3**. (c) Five photographs showing different clustering behaviours of 15  $\mu\text{L}$  water droplets on the macro-topographical feature at five different  $d$ 's. This FLIPS used diluted ferrofluid and hence did not have a micro-topographical area (see **Extended Data Fig. 3e**). See also **Supplementary Video 4**. (d) Schematic showing the unwrapping of a thin ferrofluid layer around a water droplet by changing the surrounding medium from air to a hydrocarbon. The three phases are 1-air, 1'-a hydrocarbon, 2-water, and 3-ferrofluid. (e) Five photographs showing the unwrapping of a thin layer of ferrofluid around a water droplet after the addition of dodecane. See **Supplementary Video 5**. (f) Four photographs showing

the delayed mixing of two liquid droplets in the presence of wrapping layers. The white droplet is the suspension of 10  $\mu\text{m}$  polystyrene colloids in ethanol, and the red droplet is the suspension of 10  $\mu\text{m}$  polystyrene colloids in water dyed with Rhodamine B. They were brought together by a stationary alternating current (AC) electromagnet at the center beneath the FLIPS. **(g)** Three photographs showing instant mixing of two droplets in the absence of wrapping layers. The left droplet is an aqueous solution of sodium bicarbonate, and the right droplet is an aqueous solution of 2M hydrochloric acid. The right image shows the  $\text{CO}_2$  bubble formed as a result of the droplets' coalescence. See **Supplementary Video 6**.

Another droplet manipulation strategy involves the control over the formation of the ferrofluid wrapping layer around the droplets. For example, by replacing air with an alternative liquid medium that is immiscible with the ferrofluid or the droplets, such as a hydrocarbon, the non-transparent ferrofluid wrapping layer around the water droplets can be removed (**Fig. 3e** and **Supplementary Video 5**). The unwrapping can be used to accelerate the coalescence of droplets: compared with the wrapped droplets with the mixing delayed by  $>10$  s (**Fig. 3f**), the unwrapped droplets mix instantaneously (**Fig. 3g** and **Supplementary Video 6**), allowing for rapid initiation of chemical reactions. (We note that while existing theory suggests that the formation of a wrapping layer is due to a positive spreading coefficient<sup>11,22</sup>, we found that long range van der Waals interaction is likely to be the decisive force in determining the presence or absence of the wrapping layers; see detailed discussion in **Supplementary Section III** and **Extended Data Tables 1-4** and **Figs 4-5**)<sup>23-25</sup>.

Finally, we illustrate the versatility of FLIPS at the centimeter scale by demonstrating their functions in switchable adhesion and friction, liquid pumping, and biofilm removal. We measure the adhesion between FLIPS and another surface by first pressing the test surface against FLIPS and then lifting it. With the field on, deforming the macroscopic protuberances and driving the ferrofluid back into the porous matrix requires external work. Conversely, from an energy viewpoint, the formation of the macroscopic protuberance is favored and can spontaneously open a gap between FLIPS and test surface, which enables switchable adhesion (**Fig. 4a**, **Supplementary Video 7**, and **Extended Data Fig. 6a-c**) and friction (**Supplementary Video 8**). Notably, in contrast to traditional ferrofluid-coated unstructured surfaces, FLIPS display area-specific adhesion and friction: regions with flat ferrofluid, with macrostructured protuberances and micro-topography have characteristically different values (**Extended Data Fig. 6d-h**). Furthermore, anisotropic geometry and arrangement of microstructures introduce directionality to friction that can be magnetically controlled (**Extended Data Fig. 6i**) to create unique tunable anisotropic friction materials.

Secondly, by coupling magnets' ability to extract ferrofluid from microporous structures and the movement of the magnets, we demonstrate pumping liquids at centimeter scale (**Fig. 4b** and **Supplementary Video 9**). We infused a porous polytetrafluoroethylene (PTFE) tube with ferrofluid to form a FLIPS pipe. A stepper motor moves five pairs of magnets in circular motion. The ferrofluid between each pair of magnets moves as the magnets rotate and push the test liquid along the tube. The porosity of the PTFE tube wall allows the ferrofluid to follow the circular motion of the pairs of magnets, resulting in continuous pumping enabled by a simple rotation without any complex sequential movement of magnets described earlier<sup>26</sup>. Lastly, using biocompatible fluorocarbon-based ferrofluid, we demonstrate biofilm removal on FLIPS (**Fig. 4c**). We cultured the algae biofilm on FLIPS under quiescent conditions for about a week, and then

moved a magnet under FLIPS and used the macroscopic protuberance to disrupt the green algae biofilm and detach it from the surface (**Supplementary Video 10**).

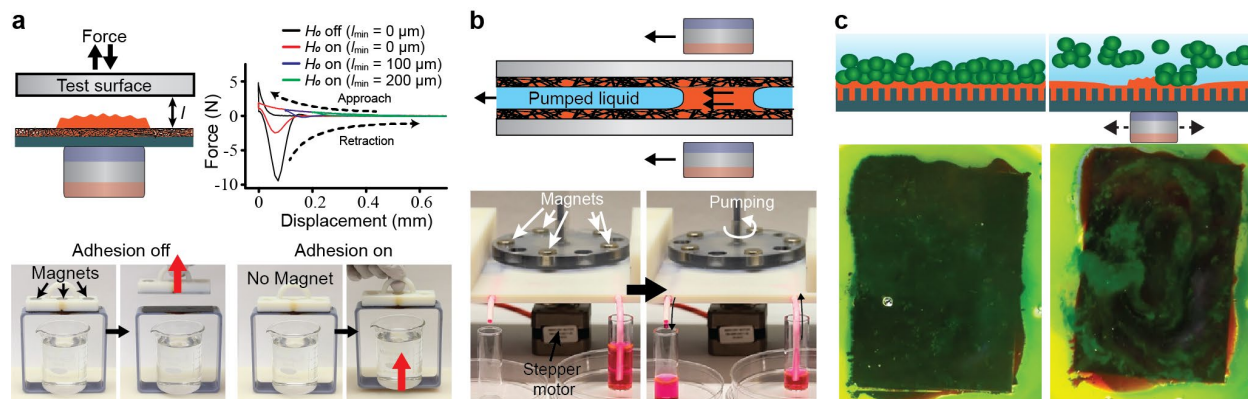


**Figure 4. Applications of FLIPS at the centimeter scale: adhesion, pumping, and biofilm removal. (a)** Adhesion: The top left schematic shows the setup for adhesion measurement. The test surface is brought in contact with FLIPS at a speed of 0.1 mm/s, held still for 10 s, and then lifted at 1 mm/s. An example of the resulting force vs distance curve is shown on the top right. The test surface in this example is a smooth PTFE. The photographs at the bottom demonstrate switchable adhesion. See **Supplementary Video 7**. **(b)** Pumping: the top is the schematic of the pumping mechanism. The pair of magnets moves the ferrofluid plug along the FLIPS pipe, which in turn drives the liquid (blue) flow inside the pipe. The bottom photographs show that an ethanol solution of Rhodamine B is pumped from the right vial to the left vial. See **Supplementary Video 9**. **(c)** The green algae biofilm is removed by swirling a magnet under FLIPS. Note that the ferrofluids used in these experiments are not toxic (See **Supplementary Section I(I)** and **Video 10**).

The multiscale topographical response of FLIPS not only possesses intriguing spatial and temporal fluid dynamics features by itself but also provides a wide range of interesting phenomena and novel functions when interfaced with other solids and liquids. Our results suggest that FLIPS allows much more diverse combinations of functional capabilities than surfaces having only a simple, single-scale topographical response<sup>11-13</sup>. The demonstrated applications—new forms of reversible, hierarchical colloidal self-assembly, manipulation and transport of non-magnetic matter in a magnetic field enabled by topography-induced hydrodynamic forces, controlled formation of droplet clusters of well-defined size, switchable adhesion and droplet motion—are only a small representative subset of these capabilities. We emphasize the broad customizability of the FLIPS topographical reconfigurations that can be tuned by changing the magnetic field, ferrofluid and, especially, the geometry and orientation of the confining microstructured surface, which in itself can be made dynamic by using flexible microstructures<sup>8,27</sup>. Our mechanistic insights gained in understanding the governing physical forces in these phenomena and ensuing functions can be readily applied to other technologically relevant developments; for example, to explore the influence of surface topography on turbulent flow<sup>28</sup>, to explore the use of the magneto-caloric effect<sup>15</sup> to manage heat transfer with its surrounding system<sup>29</sup>, and to explore the minimization of the pump for novel microfluidics platforms<sup>30</sup>. Last but not least, we expect the concept of dynamically reconfigurable multiscale topographies to find uses in biology, such as controlling and stimulating living matter simultaneously at multiple length scales<sup>31,32</sup>. We anticipate that FLIPS and its future developments will benefit such areas as responsive coatings, digital microfluidics, and biological tissue interface with dynamic materials.

**Methods** Detailed experimental protocols are included in the Supplementary Information file.

**Acknowledgements** We thank J.C. Weaver for his assistance with 3D printing, M. Khan for his assistance with preparing micro-textured silicon master, P. Kim and J. Alvarenga for their assistance with force measurements, K. Davey at American Electromechanics for his assistance with designing the electromagnet, N. Vogel, I. Morrison, Y. Hu, P. Kim, D. Daniel, M. Kreder, and O. Ahanotu for discussions. W.W. thanks Humboldt foundation for a fellowship. J.V.I.T. was supported by the European Commission through the Seventh Framework Programme (FP7) project DynaSLIPS (project number 626954). This work is supported by DOE under award # DE-SC0005247 (experiment) and by the NSF under award # DMREF-1533985 (theory). This work was performed in part at the Center for Nanoscale Systems at Harvard University (CNS), which is supported by the NSF under award # ECS-0335765.

**Author contributions** J.A., W.W., and J.V.I.T. designed the experiments. W.W. performed the experiments on dynamics of micro-topography, droplet manipulation and wrapping-layer related calculations, and pumping. J.V.I.T. performed experiments with magnet arrays, and manipulation of colloids. C.T.Y.Z fabricated the microstructures. D.D. measured the ferrofluid overlayer thickness. D.D., M.S. and W.W. performed adhesion and friction measurements. S.Ko. and J.V.I.T. performed biofilm experiments. L.M., A.C., W.W., and J.V.I.T. performed the scaling analysis. A.G. assisted in the design of experiments. S.Ke. and J.C. assisted in droplet experiments. R.T.B. assisted in the pump design. T.-S.W, B.D.H., and S.H.K. contributed to the initial conception of the project. J.A., W.W., J.V.I.T., A.G., and A.C. wrote the manuscript. J.A. supervised the research.

**Author information** The authors declare no competing conflict of interest. Correspondence and requests for materials should be addressed to J.A. (jaiz@seas.harvard.edu).

## References

- 1 Vaia, R. & Baur, J. Adaptive composites. *Science* **319**, 420-421 (2008).
- 2 Kuroki, H., Tokarev, I. & Minko, S. Responsive surfaces for life science applications. *Annu. Rev. Mater. Res.* **42**, 343-372 (2012).
- 3 Yoshida, R. Self-oscillating gels driven by the Belousov-Zhabotinsky reaction as novel smart materials. *Adv. Mater.* **22**, 3463-3483 (2010).
- 4 Reddy, S., Arzt, E. & del Campo, A. Bioinspired surfaces with switchable adhesion. *Adv. Mater.* **19**, 3833-3837 (2007).
- 5 van Oosten, C. L., Bastiaansen, C. W. M. & Broer, D. J. Printed artificial cilia from liquid-crystal network actuators modularly driven by light. *Nat. Mater.* **8**, 677-682 (2009).
- 6 Liu, D., Liu, L., Onck, P. R. & Broer, D. J. Reverse switching of surface roughness in a self-organized polydomain liquid crystal coating. *Proc. Natl. Acad. Sci. U.S.A.* **112**, 3880-3885 (2015).
- 7 Liu, D. & Broer, D. J. New insights into photoactivated volume generation boost surface morphing in liquid crystal coatings. *Nat. Commun.* **6**, 8334 (2015).
- 8 Sidorenko, A., Krupenkin, T., Taylor, A., Fratzl, P. & Aizenberg, J. Reversible switching of hydrogel-actuated nanostructures into complex micropatterns. *Science* **315**, 487-490 (2007).
- 9 He, X. M. *et al.* Synthetic homeostatic materials with chemo-mechano-chemical self-regulation. *Nature* **487**, 214-218 (2012).

- 10 Aizenberg, J., Hatton, B., Yao, X., Aizenberg, M. & Wang, W. Dynamic and switchable slippery surfaces. US9683197B2 (2017).
- 11 Khalil, K. S., Mahmoudi, S. R., Abu-dheir, N. & Varanasi, K. K. Active surfaces: Ferrofluid-impregnated surfaces for active manipulation of droplets. *Appl. Phys. Lett.* **105** (2014).
- 12 Tian, D. *et al.* Fast responsive and controllable liquid transport on a magnetic fluid/nanoarray composite interface. *ACS Nano* **10**, 6220-6226 (2016).
- 13 Irajizad, P., Hasnain, M., Farokhnia, N., Sajadi, S. M. & Ghasemi, H. Magnetic slippery extreme icephobic surfaces. *Nat. Commun.* **7**, 13395 (2016).
- 14 Xia, F. & Jiang, L. Bio-inspired, smart, multiscale interfacial materials. *Adv. Mater.* **20**, 2842-2858 (2008).
- 15 Rosensweig, R. E. *Ferrohydrodynamics*. (Dover Publications, 1997).
- 16 Rosensweig, R. E. Magnetic Fluids. *Sci Am* **247**, 136 (1982).
- 17 Odenbach, S. in *Lecture Notes in Physics: Colloidal Magnetic Fluids: Basics, Development and Application of Ferrofluids* (Springer-Verlag Berlin Heidelberg, 2009).
- 18 Timonen, J. V. I., Latikka, M., Leibler, L., Ras, R. H. A. & Ikkala, O. Switchable static and dynamic self-assembly of magnetic droplets on superhydrophobic surfaces. *Science* **341**, 253-257 (2013).
- 19 Torres-Diaz, I. & Rinaldi, C. Recent progress in ferrofluids research: novel applications of magnetically controllable and tunable fluids. *Soft Matter* **10**, 8584-8602 (2014).
- 20 Timonen, J. V. I., Demirörs, A. F. & Grzybowski, B. A. Magnetofluidic tweezing of nonmagnetic colloids. *Adv. Mater.* **28**, 3453-3459 (2016).
- 21 Yao, X. *et al.* Adaptive fluid-infused porous films with tunable transparency and wettability. *Nat Mater* **12**, 529-534 (2013).
- 22 Schellenberger, F. *et al.* Direct observation of drops on slippery lubricant-infused surfaces. *Soft Matter* **11**, 7617-7626 (2015).
- 23 Parsegian, V. A. *Van der Waals Forces : a Handbook for Biologists, Chemists, Engineers, and Physicists*. (Cambridge University Press, 2006).
- 24 Israelachvili, J. N. *Intermolecular and Surface Forces*. 3rd edn, (Academic Press, 2011).
- 25 Reiter, G. *et al.* Thin film instability induced by long-range forces. *Langmuir* **15**, 2551-2558 (1999).
- 26 Hatch, A., Kamholz, A. E., Holman, G., Yager, P. & Bohringer, K. F. A ferrofluidic magnetic micropump. *J. Microelectromech. Syst.* **10**, 215-221 (2001).
- 27 Pokroy, B., Kang, S. H., Mahadevan, L. & Aizenberg, J. Self-organization of a mesoscale bristle into ordered, hierarchical helical assemblies. *Science* **323**, 237-240 (2009).
- 28 McKeon, B. J., Sharma, A. S. & Jacobi, I. Experimental manipulation of wall turbulence: A systems approach. *Phys. Fluids* **25** (2013).
- 29 Park, K.-C. *et al.* Condensation on slippery asymmetric bumps. *Nature* **531**, 78-82 (2016).
- 30 Pamme, N. Magnetism and microfluidics. *Lab Chip* **6**, 24-38 (2006).
- 31 Verho, T. *et al.* Reversible switching between superhydrophobic states on a hierarchically structured surface. *Proc. Natl. Acad. Sci. U.S.A.* **109**, 10210-10213 (2012).
- 32 Epstein, A. K., Wong, T. S., Belisle, R. A., Boggs, E. M. & Aizenberg, J. Liquid-infused structured surfaces with exceptional anti-biofouling performance. *Proc. Natl. Acad. Sci. U.S.A.* **109**, 13182-13187 (2012).

## Supplementary Information

### Table of Contents

I.	Materials and methods.....	2
	A. Materials	
	B. Microstructured substrates	
	C. Study of the dynamics of FLIPS's micro-topographical response	
	D. Applications in colloidal assembly and transport	
	E. Droplet flow control	
	F. Control of the wrapping layer formation and droplet mixing	
	G. Adhesion and friction experiments	
	H. Demonstration of pumping	
	I. Biofilm studies	
	J. Simulations and calculations.	
II.	Additional notes on the scaling relations of FLIPS' micro-topographical response.....	11
III.	Additional notes on wrapping layer formation.....	12
IV.	Extended Data Figures.....	15
	1. Microstructure geometries and new techniques for studying the dynamics of FLIPS's topographical responses.	
	2. Profiles of ferrofluid-air interfaces measured by a 3D laser scanning confocal microscope, the dependence of the scaling relations on the overlayer thickness, and draining ferrofluid along a curved path.	
	3. Simulation of magnetic pressure and the fine-tuning of magnetic and capillary pressure balance to create or conceal the micro-topography of FLIPS.	
	4. Wrapping layers around a water droplet in air and in a hydrocarbon on FLIPS and the ability for the macroscopic protuberance to hold a droplet at various tilt angles.	
	5. Calculations of van der Waals interaction energy $G_{132}$ and disjoining pressure.	
	6. Additional adhesion and friction data.	
V.	Extended Data Tables.....	21
	1. (a) Physical properties of fluorocarbon-based ferrofluids and perfluoropolyether oil (Krytox 100) provided by the manufacturers. (b) Surface and interfacial tensions of liquids used in the study	
	2. Calculations of initial spreading coefficients and comparison with experiments	
	3. Estimations of the signs of Hamaker constants $A_{132}$ and van der Waals interaction energy $G_{132}$ by combining relations and comparison with experiments	
	4. Calculation of nonretarded Hamaker constants $A_{132}$ and van der Waals interaction energy $G_{132}$ based on the Lifshitz theory and comparison with experiments	
VI.	Description of supplementary videos.....	24
VII.	Supplementary references.....	25

## I. Materials and methods

**(A) Materials.** Hexamethyldisiloxane (HMDS) was obtained from Microchem. Positive i-line photoresist megaposit SPR700-1.0 and developer microposit MF CD-26 was obtained from Microchem. Trichloro(1H,1H,2H,2H-perfluorooctyl)silane (13F-silane) was obtained from Sigma-Aldrich. Sylgard 184 silicone (PDMS) elastomer kit was obtained from Dow Corning. UV curable epoxies (EPO-TEK OG142 and OG178) were obtained from Epoxy Technology. Polytetrafluoroethylene (PTFE) membranes with average pore sizes of 1, 10, or 20  $\mu\text{m}$  were obtained from Sterlitech and used as received. Aeos extruded microporous ePTFE tubing (ID 0.0775'' and wall thickness 0.034'', internodal distance 5 – 60  $\mu\text{m}$ ) was obtained from Zeus Inc. and used as received. Neodymium magnets (surface fields 1000 – 5000 G) were obtained from K&J magnets or Supermagnete. Alnico magnets were obtained from All Magnetics. Fluorocarbon-based ferrofluids were obtained from Ferrotec. The perfluoropolyether oil used in the dilution of ferrofluids was Dupont Krytox 100, obtained from 3M. Extended Data Table 1a summarizes the physical properties of the two types of fluorocarbon-based ferrofluids used in our experiments as well as the properties of Krytox 100. Reagent plus grade dodecane was obtained from Sigma-Aldrich.

The silicone oil-based ferrofluid was synthesized by the coprecipitation method. Briefly, 720 mL of milli-Q water was mixed with 21.6 g of iron(III) chloride hexahydrate and 11.2 g of iron(II) sulfate heptahydrate, followed by coprecipitation by adding 80 mL of ammonium hydroxide (28-30%). The formed iron oxide nanoparticles were functionalized by adding 25 g of monocarboxydecyl-terminated polydimethylsiloxane (Gelest MCR-B12) and allowing it to react overnight. Particles were purified by sedimenting them with a strong magnet, followed by removal of the aqueous supernatant and adding 400 mL of acetone to redisperse the particles. Particles were further magnetically sedimented, acetone supernatant discarded, and 250 mL of toluene added. Particles were again magnetically sedimented and toluene supernatant removed. Finally, 50 mL of toluene was added and any remaining traces of acetone were removed by heating to 60  $^{\circ}\text{C}$  for a few hours. The resulting volume of the ferrofluid in toluene was approximately 80 mL. Finally, iron oxide particles were transferred to silicone oil by mixing the nanoparticle dispersion in toluene with silicone oil and evaporating the toluene. Both fluorocarbon-based and silicone oil-based ferrofluids allow qualitatively similar results.

The preparations of different FLIPS and additional materials for specific experiments are described in detail in each section.

**(B) Microstructured substrates:** Microstructured silicon substrates (masters) were fabricated using Bosch process and replicated using soft lithography based on previous protocols<sup>1,2</sup>. Briefly, adhesion promoter (HMDS) and positive i-line photoresist (SPR700-1.0,  $\sim 2$   $\mu\text{m}$  height) were spincoated onto a clean wafer, soft-baked at 95  $^{\circ}\text{C}$  for 60 s, patterned using a direct write laser tool (Heidelberg, Maskless Aligner, 405 nm laser at  $\sim 125$   $\text{mJ}/\text{cm}^2\text{s}$ ), hardened at 115  $^{\circ}\text{C}$  for 60 s, and developed in the developer CD-26 for  $\sim 90$  s. The photoresist-patterned silicon wafer was then ion-etched under optimized Bosch conditions (SPTS Technologies) to nominal height and rinsed in acetone/isopropanol to remove residual photoresist. The resulting silicon microstructures were treated with plasma and passivated with 13F-silane under vacuum for  $>6$  h. The silicon masters were then used to prepare polydimethylsiloxane (PDMS) negative molds. PDMS prepolymer (base to hardener ratio = 10:1, wt/wt) was poured onto the master, cured at 70  $^{\circ}\text{C}$  for 2 h, and peeled

from the masters to obtain negative molds. PDMS negative molds were stored in 13F-silane vapor environment for > 3 h. The PDMS molds were then used to create epoxy positive replica. A few milliliters of epoxy (EPO-TEK OG142 or OG178) were cast at the center of a petri dish using a plastic pipette. A PDMS mold was then carefully placed over the epoxy to prevent bubbles from forming between PDMS and the epoxy layer. To obtain epoxy replicas with areas smaller than PDMS molds, a few drops of epoxy (<1 mL) was cast on PDMS mold, and a clean glass slide (rinsed with acetone, isopropanol, and water, and blow-dried with nitrogen) was slowly placed over the epoxy, followed by curing under UV light (Bio-Link 365, Vilber) for 20 min. The PDMS mold was then peeled off slowly to give the microstructured positive epoxy replica. Any variations of the procedures for preparing positive epoxy replicas are described in the respective sections.

**(C) Study of the dynamics of FLIPS's micro-topographical response.** The silicon masters are prepared on 4-inch wafers (area  $\sim 80 \text{ cm}^2$ ). Epoxy replica were made inside a 13.5-cm-diameter petri dish. To prepare FLIPS, 0.4 mL of fluorocarbon-based ferrofluid 1 was dropped onto the epoxy microstructures and spread over the substrate surface with a magnet. To vary the overlayer thickness, the FLIPS sample was spun at 500 rpm for a period of 1–5 min, and the overlayer thickness was directly measured using a force probe (see below). At the beginning of each experiment, magnets were fixed to the back of the petri dish using double-sided tape. For the data presented in **Fig. 1d** and **Extended Data Fig. 2c**, a 10-mm-diameter and 40-mm-tall N45 NdFeB magnet were used. In other control experiments, a  $\frac{1}{2}$ -inch-diameter and  $\frac{1}{2}$ -inch-tall N52 NdFeB or a 4-mm-diameter and 7-mm-tall N45 NdFeB was used. The dynamics of micro-topographical response was recorded using an angled illumination technique (see below). The videos were then analyzed using a custom Matlab code. The color thresholding was performed on V values in the HSV color space. In the experiments with the spiral pattern, a 4-mm-diameter and 7-mm-tall N45 NdFeB was used.

*Angled illumination technique (Extended Data Fig. 1b).* A cold LED line light (Zeiss CL 6000) was used to illuminate the FLIPS sample at an approximately 30 degree incidence angle. A video camera (Sony HDR CX900) was positioned directly above the FLIPS sample to record the process. Scattered light from the micro-topographical regions greatly increased the brightness of the region, and facilitated the video processing step of the analysis.

*Force probe technique to measure ferrofluid overlayer thickness (Extended Data Fig. 1c).* A spherical glass probe was lowered on the FLIPS surface at a controlled speed of  $10 \mu\text{m/s}$ . Force was recorded at 1 ms intervals using a load cell (Transducer Techniques). The probe was programmed to stop when a contact force of 50 mN was reached. The thickness of the ferrofluid overlayer was then determined from the resulting force vs displacement curve as the distance between capillary snap-in and the position where the probe touches the top of the microstructure.

*Measurement of 3D profiles of the ferrofluid-air interface.* The 3D profiles of the ferrofluid-air interface was measured using a 3D laser scanning confocal microscope (Keyence) with a 100x long working distance objective. For the data on the evolution of 3D profiles over time and the change of profiles along the x-axis (**Fig. 1c** and **Extended Data Fig. 2**), the microstructured substrates used were epoxy replicas of Pattern #1 fabricated on a 1 inch by 3 inch glass slide, with the microchannels aligned parallel to the long edge of the glass slide, and fluorocarbon-based ferrofluid 1 was used. A 4-mm-diameter and 7-mm-tall N45 NbFeB magnet was used. For the data on fine-tuning the balance between magnetic and capillary pressures (**Extended Data Fig. 3**), the microstructured substrates were epoxy replicas of Pattern #1 fabricated on a 1 inch by 3 inch glass

slide, with the microchannels aligned perpendicular to the long edge of the glass slide, or epoxy replicas of Pattern #5. Fluorocarbon-based ferrofluid 1 was used. The magnets used were either 10-mm-diameter 7-mm-tall N45 NdFeB magnets or ½-inch-diameter and ½-inch-tall Alnico magnets with a surface field of 0.041T.

**Topographical responses to magnet arrays.** FLIPS were prepared with epoxy replicas of the Pattern #4 on a 1 mm thick glass slide. Fluorocarbon-based Ferrofluid 1 was used to induce both micro-topographical and macro-topographical responses. Multiple small cylindrical magnets were first embedded into an acrylic sheet. The sheet was drilled with a hexagonal pattern of circular holes with a CO2 laser cutting system (Versalaser). The diameter of the holes was chosen to be slightly below the diameter of the cylindrical magnets (K&J Magnetics, NdFeB, diameter 1/16”) so that individual magnets could be mounted simply by pressing them into the holes without using any adhesives. The magnet array was placed on top of a white LED panel light and the FLIPS was lowered on top of the magnet array (to direct contact with the magnets). The depletion pattern propagation was immediately imaged with a digital camera (Panasonic DMC-GH4) equipped with a macro lens (Olympus Zuiko 60 mm).

#### **(D) Applications in colloidal assembly and transport**

*Assembly of non-magnetic colloidal particles on FLIPS.* The microplate array (Pattern #4) was created on the top of a standard 1-by-3 inch glass slide by replication molding of a silicon master. Briefly, PDMS (1:10) was cast on the silicon master, degassed under vacuum, cured at 70 °C and peeled off. The resulting negative mold was filled with UV-curable photopolymer (Norland Optical Adhesive 61) and pressed against the glass slide. Photopolymer was cured under UV light (Dymax 2000-EC) for ca. one minute and PDMS mold was peeled off. A liquid reservoir for the colloidal dispersion was created by attaching an aluminum washer ring (inner diameter ca. 20 mm, height few mm) on top of the microstructures with the same UV-curable photopolymer. The microstructures were then lubricated by adding a droplet of non-diluted fluorocarbon-based ferrofluid (Ferrotec) or silicone oil-based ferrofluid to completely cover the microplates. After the microplates were covered with ferrofluid, the ferrofluid could be locally depleted from the microstructures by applying a local magnetic field with a small permanent magnet. The reservoir was filled with a colloidal dispersion consisting of non-magnetic carboxylate-modified fluorescent (rhodamine B-marked) melamine microparticles 10 μm in diameter (Sigma-Aldrich). Colloidal particles were allowed to settle down for a few hours after which they were imaged with an upright confocal microscope (Zeiss LSM710) with water-dipping objectives (40x/1.0 and 10x/0.3). Depending on the state of the FLIPS surface, the colloids were found to assemble randomly on the 2D plane (flat ferrofluid-water interface, Fig. 2a) or to follow the underlying microstructure, forming particle chains (partially depleted structures in micro-topographical area, Fig 2b).

*Hierarchical assembly.* More complicated colloidal assemblies were created by using magnetically patterned FLIPS surfaces. The FLIPS substrates were created in the same way as described in the **Assembly of non-magnetic colloidal particles on FLIPS**, with the exception that a hexagonal nickel grid (Gilder hexagonal grid 100 mesh, Ted Pella Inc.) was placed between the glass slide and the PDMS mold filled with photopolymer before curing it with UV light, resulting in a microplate array with a magnetic grid under it (Fig. 2 h). If no microplates were desired (i.e. plain flat surface), a flat PDMS block was used (Fig. 2g). Lubrication and colloidal assembly were carried out as described in the previous section.

*Transport of non-magnetic colloids on FLIPS.* Magnetically induced motion of the non-magnetic colloids was demonstrated by applying a horizontal magnetic field gradient on the colloids that had settled on a partially depleted micro-topographical area of FLIPS. A gradient was created by placing an NdFeB magnet (cube, ca. 1 inch sides) next to the substrate and imaging was done with a long working distance zoom microscope (Zeiss AxioZoom). Motion of the colloids was stopped by removing the magnet (Fig. 2c-f).

### **(E) Droplet flow control**

*Effect of micro-topography.* FLIPSs were prepared with microstructured epoxy replicas of Pattern #4 for the first part of the demonstration, and Pattern #1 for the second part of the demonstration. For the second part of the demonstration, the angled illumination technique was used to visualize directly the micro-topographical region. Fluorocarbon-based ferrofluid 1 was used in order to induce a micro-topographical response. FLIPS was placed at a tilt angle of  $15 - 30^\circ$  so as to induce droplet flow due to gravity. A stack of permanent magnets (three to four of  $\frac{1}{2}$ -inch diameter and  $\frac{1}{2}$ -inch tall N52 NdFeB for the first demonstration and five of 4-mm-diameter and 7-mm-tall for the second demonstration) was placed on the top of a linear actuator (Firgelli L12P Linear Actuator w/ LAC); use of a stack of magnets helps to extend the magnetic field along the z-direction. The linear actuator has an actuation range of 10 cm, and was used to adjust precisely the relative vertical position of the magnets with respect to FLIPS. During an experiment, the magnets were first brought close to FLIPS with the separation distance in the range of  $\sim 1$  mm in order to induce a micro-topographical response. After the micro-topographical region was formed, usually after  $\sim 30$  min, a droplet of water ( $5-10 \mu\text{L}$ ) was placed in the area above the micro-topographical region so that it would begin to slide down due to gravity. Once the droplet moved into the micro-topographical region, it slowed down and eventually stopped. The magnets were lowered to a distance  $10 - 20$  mm below FLIPS so that the ferrofluid could flow back to the micro-topographical region, allowing the droplet to begin sliding again.

*Effect of macro-topography.* FLIPSs were prepared with microstructured epoxy replicas of Pattern #4. Fluorocarbon-based ferrofluid 2 was diluted to 4% by volume with Krytox 100 in order to reduce the magnetic pressure and suppress the micro-topographical response. A stack of permanent magnets (three – four  $\frac{1}{2}$ -inch diameter and  $\frac{1}{2}$ -inch tall N52 NdFeB) was placed on the top of a linear actuator (Firgelli L12P Linear Actuator w/ LAC). The linear actuator has an actuation range of 10 cm, and was used to adjust precisely the relative vertical position of the magnets with respect to FLIPS. Furthermore, the linear actuator was attached to a translational stage that was adapted and modified from the x-stage of the 3D printer RepRapPro Huxley. Both the x-stage and the linear actuator were controlled through a PC-interface. In the experiment, the magnets were first brought close to the FLIPS at about 1 mm separation distance to form the macro-topographical protuberance. A syringe equipped with a needle, pumped by a syringe pump, was positioned at the top of the FLIPS to introduce a flow of droplets. The magnets were then translated in the horizontal direction to move the macroscopic protuberance into the track of the droplet flow in order to induce droplet pinning. The magnets were then lowered successively to the desired distance from FLIPS,  $1 - 5$  mm, in order to induce different assembling behaviours of droplets.

### **(F) Control of the wrapping layer formation and droplet mixing**

*Interfacial tension measurements.* Surface and interfacial tension measurements of various liquids used in the study were performed on KSV Instruments's CAM 101 system using the pendant drop

method. Deionized water with a resistivity of  $>18.2 \text{ M}\Omega \cdot \text{cm}$  was collected from Millipore's Milli-Q water system. Dodecane of analytical standard grade (AS,  $>99.8\%$ ) and reagent plus grade (RP,  $>99\%$ ) were obtained from Sigma-Aldrich; dodecane of 99+% grade was obtained from Alfa Aesar.

*Formation and removal of wrapping layers.* FLIPS was prepared on porous PTFE membranes with  $1 \mu\text{m}$  pore size in order to suppress the micro-topographical response. Fluorocarbon-based ferrofluids and their 4% by volume dilution by the fluorocarbon oil Krytox 100 were used in the experiments to study the wrapping layer in order to avoid mixing between the ferrofluid and the content of the droplets. For the experiments shown in the video, ferrofluid 2 was used. A camera (Cannon Repel T2i) was used to record the experiment. For the formation of the wrapping layer, a water droplet was slowly placed on the FLIPS in air. For the removal of the wrapping layer, the FLIPS and the water droplet were placed in a beaker, into which a hydrocarbon was slowly added.

*Mixing droplets with wrapping layers.* FLIPS was prepared on porous PTFE membranes with  $1 \mu\text{m}$  pore size in order to suppress the micro-topographical response. Fluorocarbon-based ferrofluid 2 diluted to 4% by volume with Krytox 100 was used. The electromagnet in this experiment consisted of 286 turns of a heavy film #14 AWG wire wrapped around a  $2.61 \text{ cm} \times 0.9 \text{ cm}$  diameter iron-cobalt-vanadium Hiperco® 50 alloy core (custom fabrication from Dura Magnetics, Inc., Sylvania, OH). This electromagnet was designed to operate between 1 and 550 Hz, producing nonhysteretic  $> 0.2\text{T}$  sinusoidal magnetic fields when powered using an APS-1102 programmable AC/DC power source (Instek America Corp., Chino, CA). In the experiment, two droplets of colloidal suspensions ( $10 \mu\text{L}$  each) were placed on either side of the center of the electromagnet. One of the droplets was dyed with Rhodamine B to induce visual differences. Upon turning on the electromagnets, the droplets move and mix on the top of the alloy core of the electromagnet. A LED light was used to provide enough illumination for video recording (Cannon Repel T2i).

*Mixing droplets without wrapping layers.* FLIPS was prepared on porous PTFE membranes with  $1 \mu\text{m}$  pore size in order to suppress the micro-topographical response. The fluorocarbon-based ferrofluid 2 diluted to 4% by volume with Krytox 100 was used. The FLIPS was placed in a plastic Petri dish, which was then filled with dodecane. Droplets ( $\sim 10 \mu\text{L}$ ) of aqueous solution of sodium bicarbonate and hydrogen chloride were then placed on the FLIPS with a micro-pipette. A permanent magnet was used to induce a macroscopic response in order to push one droplet towards the other droplet and mix them.

## **(G) Adhesion and friction experiments**

*Adhesion measurements on PTFE-membrane-based FLIPS.* FLIPS was prepared with porous PTFE membrane with  $20 \mu\text{m}$  pore size and fluorocarbon-based ferrofluid 1 and 2 without dilution in order to induce both micro-topographical and macro-topographical responses. As a result, the size of the macro-topographical protuberance and its ability to spontaneously separate two surfaces was influenced not only by the ferrofluid overlayer but also by the amount of ferrofluid extracted from the porous membrane. Adhesion measurements were performed on an Instron 5566 electromechanical testing system. A plastic sample holder was designed and 3D printed to fit the gripper of the instrument and to provide a flat top surface with an area of one square inch. The porous PTFE membrane was first attached to the top of the 3D printed sample holder with double-sided tape, and then  $150 \mu\text{L}$  of ferrofluid was added. Glass cover slide, polytetrafluoroethylene Teflon sheet (McMaster Carr, 0.015-inch thick, one side adhesive ready), and SLIPS were attached

to another sample holder. FLIPS was positioned at the bottom, and the test surface at the top. During testing, the FLIPS stayed stationary, and the test surface was first brought down at a speed of 0.1 mm/s to be in contact with FLIPS, held still for 10 s, and then retracted at 0.01, 0.1 or 1 mm/s. Position  $l = 0$  corresponds to the position where the top surface was pressed slightly against FLIPS without squeezing ferrofluid out of FLIPS. For each data point, a minimum of five measurements were performed.

*Adhesion measurements on channel-like microstructure-based FLIPS.* The microstructure of Pattern #1 was used to demonstrate anisotropic properties of FLIPS. The substrates were prepared with glass slide backing. Epoxy (EPO-TEK OG178) was cast onto the PDMS mold, and the glass slide was placed onto the epoxy, creating a homogeneous thin epoxy layer between the PDMS mold and the glass slide, and cured under UV light. The microstructured epoxy resin was then peeled off the mold, infiltrated with 100  $\mu\text{L}$  of fluorocarbon-based ferrofluid 1 and spun at 500 rpm for 60 s before being attached to another sample holder. The overlayer thickness was estimated to be  $\sim 20 \mu\text{m}$ . The adhesion measurements were performed on a customized setup. The adhesion setup was built on an inverted optical microscope (Axio Observer A1, Zeiss) with a video camera (Grasshopper<sup>®</sup>3, Point Grey Research Inc.), enabling the recording of the contact interface. The adhesion force was measured by a sensitive load cell (GSO-25 and -1K, Transducer Techniques<sup>®</sup>) mounted on a computer-controlled high-precision piezo motion stage (LPS-65 2", Physik Instrumente GmbH & Co. KG) in the z-direction, with a resolution of 5 nm and a maximum velocity of  $10 \text{ mm}\cdot\text{s}^{-1}$ . Fine positioning in the x- and y-directions was done by a manual xy-stage (NFP-2462CC, Positionierungstechnik Dr. Meierling) and tilt correction was adjusted by two goniometers (M-GON65-U, Newport). Motion control of the piezo stages and data acquisition were performed by a customized Linux code (Ubuntu<sup>™</sup>, Canonical Ltd.). The program allowed control over preload, velocity, displacement in the x- and z-directions, and contact time. The load cell was linked to the computer *via* a signal conditioner (BNC-2110, National Instruments) and the voltage signal from the force measurement was transferred through a data acquisition board (PCIe-6259, National Instruments). A brass holder with attached plastic disk was prepared to attach the PDMS probe to the load cell. The circular plastic disk with 4 mm diameter and 1 mm thickness was laser cut from a plastic plate and attached to the brass holder by a silicone adhesion promoter (Sil-Poxy<sup>®</sup>, Smooth-On Inc.). FLIPS was positioned at the bottom, and the holder on top. Sylgard 184 prepolymer and curing agent with weight ratio of 10:1 were mixed, degassed, and cast on a glass plate, and a thin film with 500  $\mu\text{m}$  thickness was created by a film applicator (Multicator 411, Erichsen GmbH & Co. KG). The sample was cured in a vacuum oven at  $90^\circ\text{C}$  for 1 hour. Square PDMS probes with 5mm side length were cut from a 500  $\mu\text{m}$  thick PDMS film and placed onto the FLIPS surface to ensure alignment. A Vinylsiloxane polymer (Flexitime<sup>®</sup> Medium Flow, Heraeus Kulzer GmbH) was used to bond the PDMS probe to the holder. The holder was inked into the uncured Vinylsiloxane polymer film, approached and contacted with the backside of the aligned PDMS probe with 50 mN compressive load. After 3 minutes, the VS polymer was polymerized and the probe bonded to the holder. During the adhesion testing, the FLIPS stayed stationary, and the probe approached the surface at  $50 \mu\text{m/s}$  and was first brought in contact with a preload of 50 mN. After a contact time of 10 s, the probe was retracted at a speed of 10, 100 or 1000  $\mu\text{m/s}$  until the probe was detached from the FLIPS. The probe was cleaned after each measurement with a particle-free tissue and isopropanol in order to remove accumulated ferrofluid. Pristine and representative positions of the different regions ( $H_0$  off, R1, R2 and R3) were selected for each measurement. The ferrofluid was respread over the substrate surface with a magnet and the initial conditions were restored, and all pristine and representative positions were measured.

The experiments were conducted in a temperature- and humidity-controlled lab with the conditions kept at 20-25 °C and 25-35 %, respectively. For each data point, a minimum of five measurements were performed.

*Friction measurements on channel-like microstructure-based FLIPS.* FLIPS samples were prepared in the same way as in the section *Adhesion measurements on channel-like microstructure-based FLIPS*. Friction measurements were performed on the same customized setup. The load cell was attached to the z-direction piezo motion stage perpendicular to the FLIPS. A plastic holder was designed and laser cut to attach the PDMS film probe to the load cell and to provide aligned configuration. Sylgard 184 prepolymer and curing agent with a weight ratio of 10:1 were mixed, degassed, and cast on a glass plate, and a thin film with 500 μm thickness was created by a film applicator (Multicator 411, Erichsen GmbH & Co. KG). The sample was cured in a vacuum oven at 90°C for 1 hour. The PDMS film probe with length of 25 mm was cut from a 500 μm thick PDMS film. A one square centimeter PDMS piece was attached to the lower side of the film probe by a thin layer of silicone adhesion promoter to provide a constant contact area. The PDMS film probe was bonded to the plastic holder by a silicone adhesion promoter. The positioning in the x- and y-directions was done by a manual xy-stage and tilt was corrected by two goniometers in order to ensure parallel shear. During testing, the film probe stayed stationary, and FLIPS was sheared parallel at a constant velocity. The film probe approached the surface with 1000 μm/s and was brought in contact with the substrate. A constant load of 10 or 100 mN was applied. After a contact time of 10 s, the FLIPS was sheared over a distance of 500 and 1000 μm with a velocity of 100 and 1000 μm/s. The probe was cleaned after each measurement with a particle free tissue and isopropanol in order to remove accumulated ferrofluid. Pristine and representative positions of the different regions ( $H_0$  off, R1, R2 and R3) were selected for each measurement. The ferrofluid was respread over the substrate surface with a magnet and the initial conditions were restored, and all pristine and representative positions were measured. The experiments were conducted in a temperature- and humidity-controlled lab, with the conditions kept at 20–25 °C and 25–35%, respectively. For each data point, a minimum of 5 measurements were performed.

*Demonstration of switchable adhesion.* FLIPS were prepared on porous PTFE membranes with 20 μm pore size. Ferrofluid 2 was used to induce both macro-topographical and micro-topographical responses. As a result, the size of the macro-topographical protuberance and its ability to spontaneously separate two contacting surfaces was influenced not only by the ferrofluid overlayer but also by the amount of ferrofluid extracted from the porous membrane. 3D models were created in Rhinoceros 3D with the aid of Grasshopper plugin and were printed on Objet Connex 500. Before the experiment, the PTFE membrane was attached to the top of the white holding frame, and the ferrofluid was added and spread using a magnet. A beaker was then placed insides the holding frame, and the top handle was placed on FLIPS. Three separate ½-inch-diameter and ½-inch-tall N52 NbFeB magnets were introduced manually to generate a topographical response. The macro-topographical protuberance (whose size was determined not only by the ferrofluid overlayer, but also by the amount of ferrofluid extracted from the microporous membrane, i.e. the micro-topographical response) creates a gap that reduces the adhesion between the top handle and the bottom frame. The magnets were later removed with a magnetic stainless steel tweezer.

*Demonstration of switchable friction.* FLIPS were prepared on porous PTFE membranes with 20 μm pore size. Ferrofluid 2 was used to induce both macro-topographical and micro-topographical responses. As a result, the size of the macro-topographical protuberance and its ability to

spontaneously separate two contacting surfaces was influenced not only by the ferrofluid overlayer but also by the amount of ferrofluid extracted from the porous membrane. 3D models were created in Rhinoceros 3D with the aid of Grasshopper plugin and were printed on Objet Connex 500. A stepper motor (Lin Engineering, 3518M-07) was used to provide the rotation. Arduino Uno microcontroller with Adafruit motor shield was used to control the rotation of the stepper motor and interface it with a laptop PC. The 3D printed set consisted of a bottom spinning wheel that was attached to the shaft of the stepper motor, a top spinning wheel, and a top stationary wheel. PTFE membrane was first attached to the top surface of the bottom spinning wheel, and the ferrofluid was added to the middle of the membrane. The top spinning wheel was then pressed against the bottom spinning wheel in order to spread the ferrofluid uniformly throughout the PTFE membrane. Two stacks of plastic Petri dishes and several plastic sheets were used to adjust the height of the top stationary wheel in order for it to constrain the position of the top spinning wheel. Four small black parts were attached to the top spinning wheel as a visual indicator of spinning and also to adjust the overall friction during spinning. At the center of the top spinning wheel, a ½-inch wide hole was created to accommodate a stack of two ½-inch-diameter and ½-inch-tall N52 NbFeB magnets. During the demonstration, the movement of the stepper motor rotates the bottom spinning wheel, which rotates the top spinning wheel without magnets. When the magnets were placed in the hole in the top spinning wheel, the macro-topographical protuberance (whose size was determined by not only the ferrofluid overlayer, but also by the amount of ferrofluid extracted from the microporous membrane, i.e. the micro-topographical response) creates a gap that reduces the friction between the top and the bottom spinning wheels and stop the rotation of the top spinning wheel. The explanatory animation was made in Maya, using the models created in Rhinoceros 3D.

**(H) Demonstration of pumping.** Aeos extruded microporous ePTFE tubing (effective pore size  $\sim 5 - 60 \mu\text{m}$ ) and ferrofluid 2 were used to allow the ferrofluid to move in and out of the tubing pore wall. 3D-printed parts were used to construct the rest of the pump. 3D models were created in Rhinoceros 3D with the aid of Grasshopper plugin and were printed on Objet Connex 500. The stepper motor (Lin Engineering, 3518M-07) was used to provide rotation. Arduino Uno microcontroller with Adafruit motor shield was used to control the rotation of the stepper motor and interface it with a laptop PC. The 3D printed set consisted of a flat top plate and a bottom plate with a circular track and two linear tracks to accommodate the movement of the ferrofluid protuberance and the tubing, and two spinning wheels, each with 10 slots for ½-inch-diameter and ½-inch-tall magnets. Before the experiment, the ePTFE tube was first fitted into the track in the bottom plate, and the ferrofluid was added at various locations along the circular track in order to wet the tube. Krytox 100 oil was added to various locations along the linear tracks to provide sealing for the liquid being pumped along the inlet and outlet part of the tube. The top plate was then used to sandwich the tube, and the sandwich structure was then placed on the top of the bottom spinning wheel, inside which five magnets were positioned in the holes along the perimeter with even spacing. The top spinning wheel was then installed, into which another five magnets were placed. The explanatory animation was made in Maya, using models created in Rhinoceros 3D.

## **(I) Biofilm studies**

*FLIPS preparation.* PTFE membranes with a pore size of  $10 \mu\text{m}$  were adhered to a 50 mm x 75 mm glass slide using a thin layer of semi-cured PDMS (Sylgard® 184 silicone elastomer Dow Corning Corporation, Midland, MI), allowing the thorough attachment of the membrane to the

glass slide without infiltrating the PTFE network with PDMS. After completing the PDMS curing in an oven (70 °C for 4h), 500 µl of ferrofluid was added to the surface of each PTFE membrane and carefully spread using a ring magnet until all of the membrane area was fully infused with ferrofluid. Ferrofluids used in our study consisted of non-toxic components: iron oxide particles dispersed in fluorocarbon solvents. The non-toxicity of many fluorocarbon solvents is well-known and manifested by the fact that they have even been used as the main ingredients in artificial blood substitutes (Fluosol) that are FDA-approved and used with human subjects (<https://en.wikipedia.org/wiki/Fluosol>). At the same time, iron oxide nanoparticles are also non-toxic with some specific types also FDA-approved as MRI contrast agents. This is in stark contrast to ferrofluids based on many other types of carrier fluids and nanoparticles, including nickel and cobalt, which are known to be toxic towards biological matter.

*Algae cultivation and experimental setup.* The green alga *Chlamydomonas reinhardtii* (UTEX number 89) from the University of Texas Culture Collection was used as a model organism to explore the biofilm disruption / detachment potential of FLIPS systems. *C. reinhardtii* was grown in a Soil Extract (Bristol medium based) solution under non-axenic conditions until the stock culture reached a density of approximately  $1 \times 10^7$  cells ml<sup>-1</sup>. This stock culture was diluted with fresh Soil Extract to a 1:5 ratio of stock culture to fresh medium. 80 ml of the diluted culture was added to square (10 cm x 10 cm) Petri dishes containing the prepared FLIPS treatments, allowing the algae to settle on test surfaces. The Petri dishes were then placed under a Sun Blaze T5HO fluorescent light fixture (Sunlight Supply, Inc., Vancouver, WA) and were grown under a 16:8 h light-dark cycle at 24 °C for 7 days until a cohesive green algae biofilm had formed. No negative impact of the ferrofluid on algae growth and biofilm formation was observed when compared with PTFE-only control treatments, and a healthy-green algae biofilm remained stably attached to the surface until the magnetic actuation was performed, thus confirming the non-toxic nature of FLIPS.

*Biofilm removal.* To test the potential of FLIPS surfaces to disrupt / detach the adhered biofilm, a ring magnet was introduced immediately beneath the square Petri dishes containing the fouled FLIPS and the algae medium. The applied magnetic fields then led to a concentration of the ferrofluid beneath the magnet, breaking up the adhered green algae biofilm in the process. Moving the magnet up and down the slide caused a ‘ferrofluid wave’ to travel over the FLIPS, detaching and concentrating the biofilm. The aggregations of biofilms moved along with the ferrofluid wave but did not mix with the underlying ferrofluid. After removing the magnet, the Petri dishes were shaken gently to see if the biofilm remnants were still associated with the ferrofluid. The biofilm threads were not associated, but instead lifted off the FLIPS and started floating freely into the algae media. In contrast, simple shaking of the Petri dishes without magnetic actuation did not result in any biofilm detachment from the FLIPS surface. Control PTFE treatments not containing any ferrofluid showed no response to the magnetic actuations and the attached green algae biofilms remained firmly attached to the surface of the controls.

**(J) Simulations and calculations.** Simulations of magnetic fields and magnetic pressures were performed with COMSOL. The data for the ferrofluid M-H curve were obtained from Ferrotec inc. Calculation of the force density was performed with OriginLab. Calculations of van der Waals energy and disjoining pressure were performed with Mathematica.

**Data availability.** The datasets generated and/or analysed during the current study are available from the corresponding author.

## II. Additional notes on the scaling relations of FLIPS' micro-topographical response

Using the geometry in Fig. 1b, the pressure gradient in the  $x$  direction drives the flow and is resisted by the viscous dissipation in the  $z$  direction; thus using the lubrication approximation<sup>3,4</sup>, we have

$$\frac{\partial p_\gamma}{\partial x} = \eta \frac{\partial^2 U}{\partial z^2} \quad (1)$$

where  $p_\gamma \approx 2\gamma/dy$  is the capillary pressure and  $U \approx dL_x/dt \approx L_x/t$ . Physically, the left-hand-side represents the capillary pressure gradient (which drives the porous-capillary flow), and the right-hand-side represents the viscous dissipation. Using approximations  $\partial p_c/\partial x \approx p_\gamma/L_x \approx 2\gamma/dyL_x$  and  $\partial^2 U/\partial z^2 \approx U/h_0^2 \approx L_x/th_0^2$ , and rearranging terms gives the scaling relation

$$L_x \approx \left( \frac{2\gamma h_0^2}{\eta dy} \right)^{1/2} t^{1/2} \quad (2)$$

Putting numerical values in the above equation and setting units of  $L_x$  as mm and  $t$  as seconds gives  $L_x \approx 0.35t^{1/2}$ . This derivation gives the same power law as equation (2) in the main text. The only difference is the pre-factor.

A second alternative is to use magnetic pressure to replace the capillary pressure term.

$$\frac{\partial |p_m|}{\partial x} = \eta \frac{\partial^2 U}{\partial z^2} \quad (3)$$

where  $|p_m| \approx \mu_0 M_s H_0$ . Physically, this replacement represents the incorporation of the actual driving force, the magnetic pressure gradient, in the formulation of the scaling relation.

Arranging terms gives the scaling relation

$$L_x \approx \left( \frac{|p_m| h_0^2}{\eta} \right)^{\frac{1}{2}} t^{\frac{1}{2}} \quad (4)$$

Using the value  $p_m \approx 10^4$  Pa and again setting units of  $L_x$  as mm and  $t$  as seconds gives  $L_x \approx 5.6t^{1/2}$ .

The derivations in the main text and here all give the same power law, and only differ in the pre-factors. A more accurate model will need to combine these models: near the magnet, it is primarily the magnetic force that drives the flow; and far from the magnet, it is the capillary pressure gradient that drives the flow. In addition, these scaling derivations are essentially two dimensional models, and they omit the three dimensional nature of the microstructure geometry. We are currently developing numerical models to take into account all the considerations stated above.

### III. Additional notes on the wrapping layer formation.

The estimation of the formation of the wrapping layers based on the calculation of the (initial) spreading coefficients does not correlate with our experiments (**Extended Data Fig. 4** and **Table 2**). This method is derived from the work by W.B. Hardy in early 1920s.<sup>5,6</sup> It is also the method of choice in recent studies on wrapping layers.<sup>7,8</sup> We adopt the usage of the term “initial spreading coefficient”  $S_i$  to denote the value we calculate<sup>9</sup>, and reserve the term “spreading coefficient” to mean “true equilibrium spreading coefficient”.<sup>9</sup> *The main source of discrepancy for the  $S_i$  approach is that interfacial tensions are very sensitive to trace amounts of surface-active agents, especially for a water-hydrocarbon interface. Any additives such as dyes or even air-borne dust particles can alter the values of the water-hydrocarbon interfacial tensions significantly enough to change the signs of  $S_i$ 's.*

Our estimation of the formation of the wrapping layer is based on the calculations of long-range van der Waals (vdW) interactions.<sup>4,10,11</sup> The origin of this long-range vdW interaction is different from that of the surface tension (which is due to short-range intermolecular forces) and represents the interaction between the two media across the wrapping layer (hence long-range). If this interaction between the two media is attractive, then the wrapping layer is absent; if this interaction is repulsive, then the wrapping layer is formed. Knowing the sign of this interaction will enable us to estimate the stability of the wrapping layer (in other words, the absence or the presence of the wrapping layer). From the perspective of thin films, a ferrofluid thin film is stable between water and air because the repulsive vdW interaction between air and water tends to thicken it; on the other hand, a ferrofluid thin film is unstable between water and hydrocarbon because the attractive vdW interaction between water and hydrocarbon tends to thin it down.

We provide below three methods to estimate the signs of this long-range van der Waals interactions, in the order of increasing complexity: (1) estimation using combining relations (**Extended Data Table 3**), (2) estimation using non-retarded Hamaker constants based on Lifshitz theory (**Extended Data Table 4**), and (3) estimation of Hamaker constants with relativistic retardation correction based on Lifshitz theory (**Extended Data Fig. 5**).

**Method 1:** Estimating the signs of Hamaker constants  $A_{132}$  and van der Waals interaction energy  $G_{132}$  using combining relations (results are presented in **Extended Data Table 3**).

The following equations are used.<sup>11,12</sup>

$$A_{132} = (\sqrt{A_{11}} - \sqrt{A_{33}})(\sqrt{A_{22}} - \sqrt{A_{33}}) \approx 24\pi\delta_0^2 \left( \sqrt{\gamma_1^D} - \sqrt{\gamma_3^D} \right) \left( \sqrt{\gamma_2^D} - \sqrt{\gamma_3^D} \right) \quad (5)$$

$$G_{132} = -\frac{A_{132}}{12\pi d^2} \sim -\left( \sqrt{\gamma_1^D} - \sqrt{\gamma_3^D} \right) \left( \sqrt{\gamma_2^D} - \sqrt{\gamma_3^D} \right) \quad (6)$$

where  $A_{ijk}$  is the Hamaker constant for the interaction between medium  $i$  and medium  $k$  across medium  $j$ ;  $G_{ijk}$  is the van der Waals interaction energy for the interaction between medium  $i$  and medium  $k$  across medium  $j$ ;  $A_{ii}$  is the Hamaker constant for the interaction between medium  $i$  across vacuum;  $\delta_0$  is the atomic cutoff distance (constant);  $\gamma_i^D$  is the dispersive component of surface tension of medium  $i$ ;  $d$  is the thickness of the intermediate medium. For hydrocarbons and ferrofluids,  $\gamma_i^D$  is equal to their surface tensions in air; for water,  $\gamma_i^D$  is  $\sim 22$  mN/m.<sup>12,13</sup>

The calculation used the physical properties of fluorocarbon-based ferrofluids and perfluoropolyether oil (Krytox 100) provided by the manufacturers and the measured surface and interfacial tensions of liquids used in the study (**Extended Data Table 1**).

**Method 2:** Estimating non-retarded Hamaker constants  $A_{132}$  and van der Waals interaction energy  $G_{132}$  based on Lifshitz theory (results are presented in **Extended Data Table 4**)

The calculations are based on the following equation, adapted from Israelachvili, J. N. Intermolecular and surface forces. 3rd edn, 2011, Chapter13, eq. (13.15).<sup>11</sup>

$$A_{total} = A_{v=0} + A_{v>0}$$

$$\approx \frac{3}{4} kT \left( \frac{\epsilon_1 - \epsilon_3}{\epsilon_1 + \epsilon_3} \right) \left( \frac{\epsilon_2 - \epsilon_3}{\epsilon_2 + \epsilon_3} \right) + \frac{3h\nu_e}{8\sqrt{2}} \frac{(n_1^2 - n_3^2)(n_2^2 - n_3^2)}{(n_1^2 + n_3^2)^{\frac{1}{2}}(n_2^2 + n_3^2)^{\frac{1}{2}} \left[ (n_1^2 + n_3^2)^{\frac{1}{2}} + (n_2^2 + n_3^2)^{\frac{1}{2}} \right]} \quad (7)$$

$$G_{132} = -\frac{A_{132}}{12\pi d^2} \quad (8)$$

Note 1:  $A_{Total}$  is dominated by the dispersive term  $A_{v>0}$ , so we can use refractive indexes alone to predict the sign of van der Waals interaction energy in our droplet-on-FLIPS systems.

Note 2: The calculations used the dielectric constants and the refractive indices of the solvents of ferrofluids, and in the case of 4v% FF, the properties of Krytox 100. This assumption is justified on the ground that nanoparticles of iron oxides are shielded by fluorocarbon surfactants or polymers and that their van der Waals interactions with other media are thus greatly reduced. The dominant role of dispersive forces manifests itself in the surface tension of pure ferrofluid: the dispersive components of the surface tensions of ferrofluid 1 and ferrofluid 2 are estimated to be 13.7 mN/m and 12.4 mN/m, respectively, according to the equation  $\gamma_i^D = A_{ii}/24\pi(0.165 \text{ nm})^2$ .

Note 3: This method gives the same correct prediction for the formation of the wrapping layer as the method in **Extended Data Table 3**. In essence, these calculations reflect the excess polarizability, or relative polarizability of different phases. Namely, fluorocarbon is less polarizable than water or hydrocarbon, but more polarizable than air (vacuum).<sup>4,10</sup>

Note 4: Physical constants of water, dodecane, and air:  $\epsilon_{\text{water}} = 80$ ,  $n_{\text{water}} = 1.333$ ;  $\epsilon_{\text{dodecane}} = 2.01$ ,  $n_{\text{dodecane}} = 1.411$ ;  $\epsilon_{\text{air}} = 1$ ,  $n_{\text{air}} = 1$ .

**Method 3:** Estimating Hamaker Constants  $A_{132}$  with relativistic retardation correction, the van der Waals interaction energy  $G_{132}$ , and the disjoining pressure (results are presented in **Extended Data Figure 5**)

The calculations are based on the following equations, which are adapted from the section L 2.4. of Van der Waals Forces by Parsegian.<sup>10</sup>

$$\epsilon_i(i\xi_n) = 1 + \frac{n_i^2 - 1}{1 + (\xi_n/\omega_{UV})^2}, \quad i = 1, 2, 3 \quad (9)$$

$$\xi_n = \frac{2\pi kT}{\hbar} n, \quad n = 1, 2, 3, 4 \dots \quad (10)$$

$\epsilon_i(i\xi_n)$  is the dielectric response of medium  $i$  at imaginary frequencies  $i\xi_n$ , and  $\xi_n$  are sampling frequencies, or the so-called ‘‘Matsubara frequencies’’.

$$R(l) = (1 + r_n)e^{-r_n} \quad (11); \quad r_n(l) = \frac{2l}{c/\epsilon_3(i\xi_n)^{\frac{1}{2}}} \cdot \xi_n \quad (12)$$

$R(l)$  and  $r_n(l)$  accounts for the retardation of van der Waals interactions over distance  $l$  due to the finite velocity of electromagnetic waves.

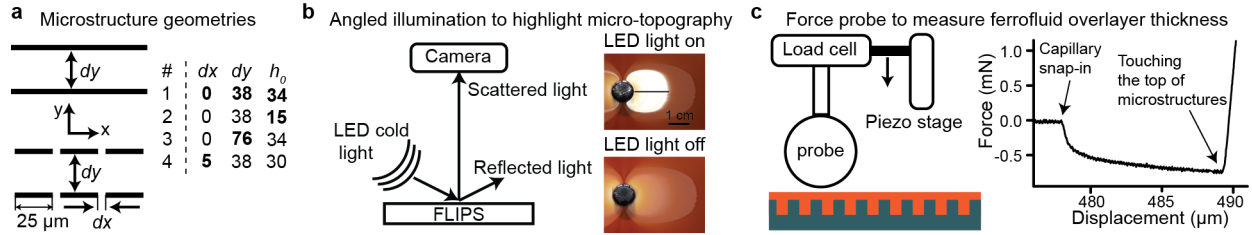
$$A_{132}(l) = \frac{3kT}{2} \sum_{\xi_n} \left( \frac{\varepsilon_1(i\xi_n) - \varepsilon_3(i\xi_n)}{\varepsilon_1(i\xi_n) + \varepsilon_3(i\xi_n)} \right) \left( \frac{\varepsilon_2(i\xi_n) - \varepsilon_3(i\xi_n)}{\varepsilon_2(i\xi_n) + \varepsilon_3(i\xi_n)} \right) \times R(l) \quad (13)$$

$$G_{132}(l) = -\frac{A_{132}(l)}{12\pi l^2} \quad (10); \quad p_{dis} = -\frac{\partial G_{132}(l)}{\partial l} \quad (14)$$

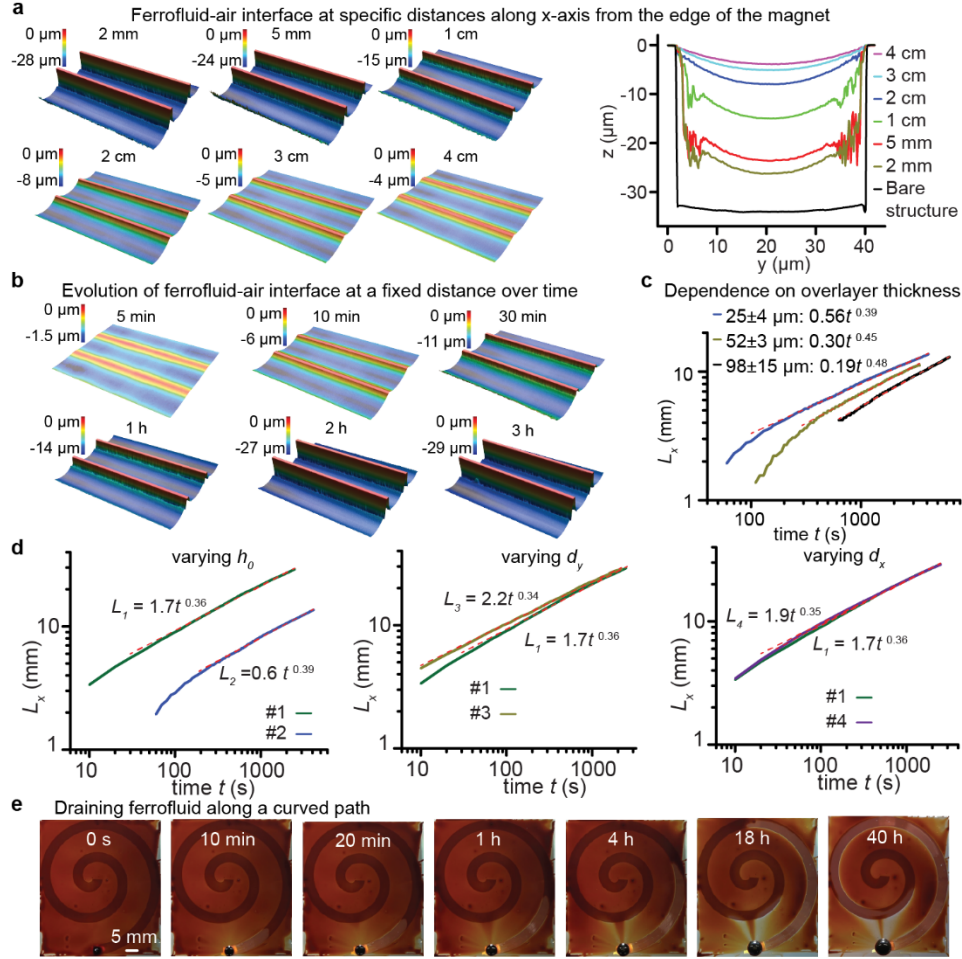
$A_{132}(l)$  is the Hamaker constant for medium configuration 1-3-2,  $G_{132}(l)$  is the corresponding van der Waals interaction energy, and  $p_{dis}$  is the corresponding disjoining pressure.

This method is most useful when one starts to study the thickness-dependent properties of wrapping layers such as meta-stability, and can be further extended to investigate the fine balances among disjoining pressure, capillary pressure, and magnetic pressure.

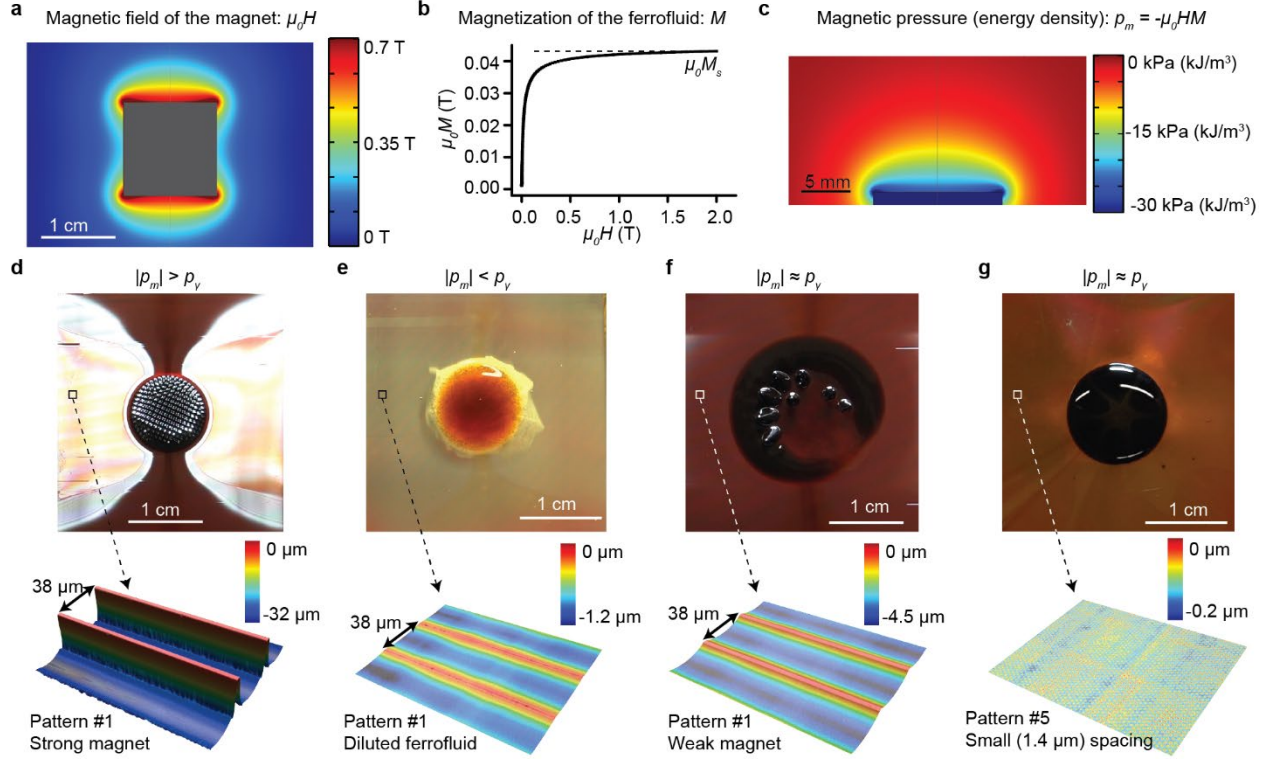
## IV. Extended Data Figures



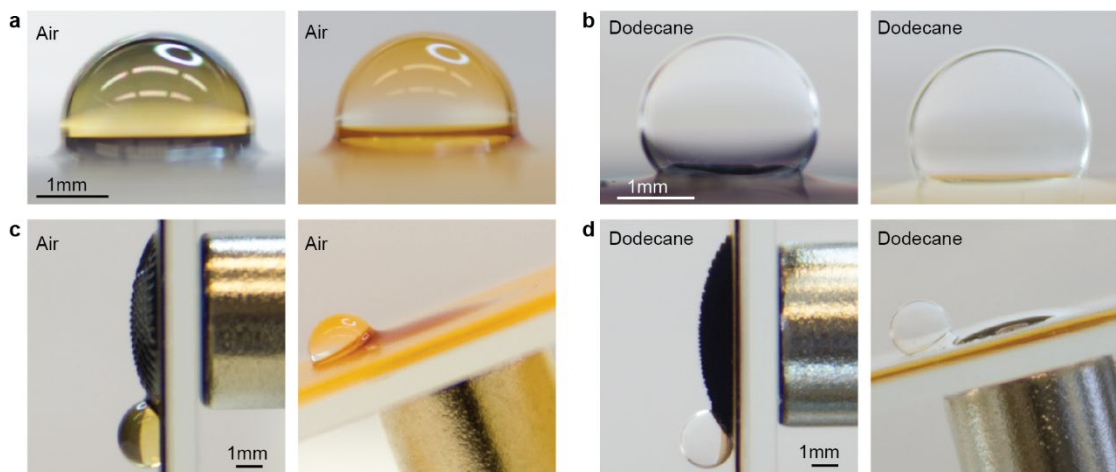
**Extended Data Figure 1. Microstructure geometries and new techniques for studying the dynamics of FLIPS's topographical responses.** (a) Microstructure geometries used in the scaling analysis of the dynamics of micro-topographical response: arrays of microchannels (#1 – 3) and array of microplates (#4). The comparisons between #1 and #2 – 4 show the influences of  $h_o$ ,  $d_y$ , and  $d_x$ , respectively. (b) Angled illumination technique to highlight the micro-topographical region. A LED cold line light (Zeiss CL 6000) illuminates the FLIPS sample from an incidence angle of  $\sim 30^\circ$  to induce scattering from the micro-topographical region. The contrast due to high brightness produced from the scattering greatly facilitates the color thresholding step in the video processing. The two images on the right show the comparison with and without the LED light. (c) Force probe technique to measure the ferrofluid overlayer thickness. The left diagram is a schematic of the setup. A spherical probe connected to a load cell is slowly lowered onto the FLIPS surface through the motion of a piezo stage. The speed of the approach ( $10 \mu\text{m/s}$ ) and the sampling rate of the load cell (1 ms) determine the resolutions of the measurement (10 nm). The plot on the right is a representative force vs. displacement curve from the measurement. The overlayer thickness is the distance between the capillary snap-in (the moment the probe touches the top of the overlayer) and the beginning of the steep increase in the force (the moment the probe touches the top of the microstructures).



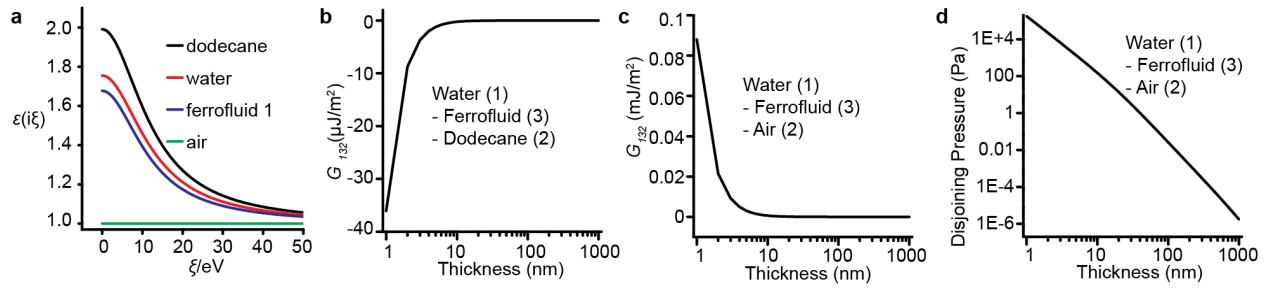
**Extended Data Figure 2. Profiles of ferrofluid-air interfaces measured by a 3D laser scanning confocal microscope, the dependence of the scaling relations on the overlayer thickness, and draining ferrofluid along a curved path.** (a) 3D profiles of ferrofluid-air interface measured along the x-axis at various distances from the edge of the magnet. The profiles show a gradual increase in the ferrofluid level inside the channel along the x-axis, which corresponds to a gradual decrease in interfacial curvature. Measurements were performed on a 1-inch by 3-inch FLIPS sample after 2 h. Pattern #1 was used, and the channel direction was aligned to the long side of the FLIPS sample. To the right is the plot of the cross-section profiles of the ferrofluid-air interface. The signal is noisy in the high curvature region near the edge, due to the limit of the numerical aperture of the 100x long-working distance objective used. (b) 3D profiles of ferrofluid-air interface measured 1.5 cm away from the edge of the magnet over time. The FLIPS sample is the same as in (a). The profiles show a gradual decrease of ferrofluid level inside the channel, which corresponds to a gradual increase of the ferrofluid-air interface curvatures. The corresponding plots of the cross-section profiles are presented in Fig. 1c. (c) Dependence of the scaling relations on the overlayer thickness. Pattern #2 was used. Increasing overlayer thickness decreases the prefactor but increases the power in the scaling relations. (d) Effects of varying  $h_0$ ,  $d_y$ , and  $d_x$  on scaling relations. The overlayer thicknesses are  $\sim 10$ – $20 \mu\text{m}$ . (e) Draining ferrofluid along a curved path in a spiral pattern, demonstrating the ability of the porous-capillary flow to make turns.



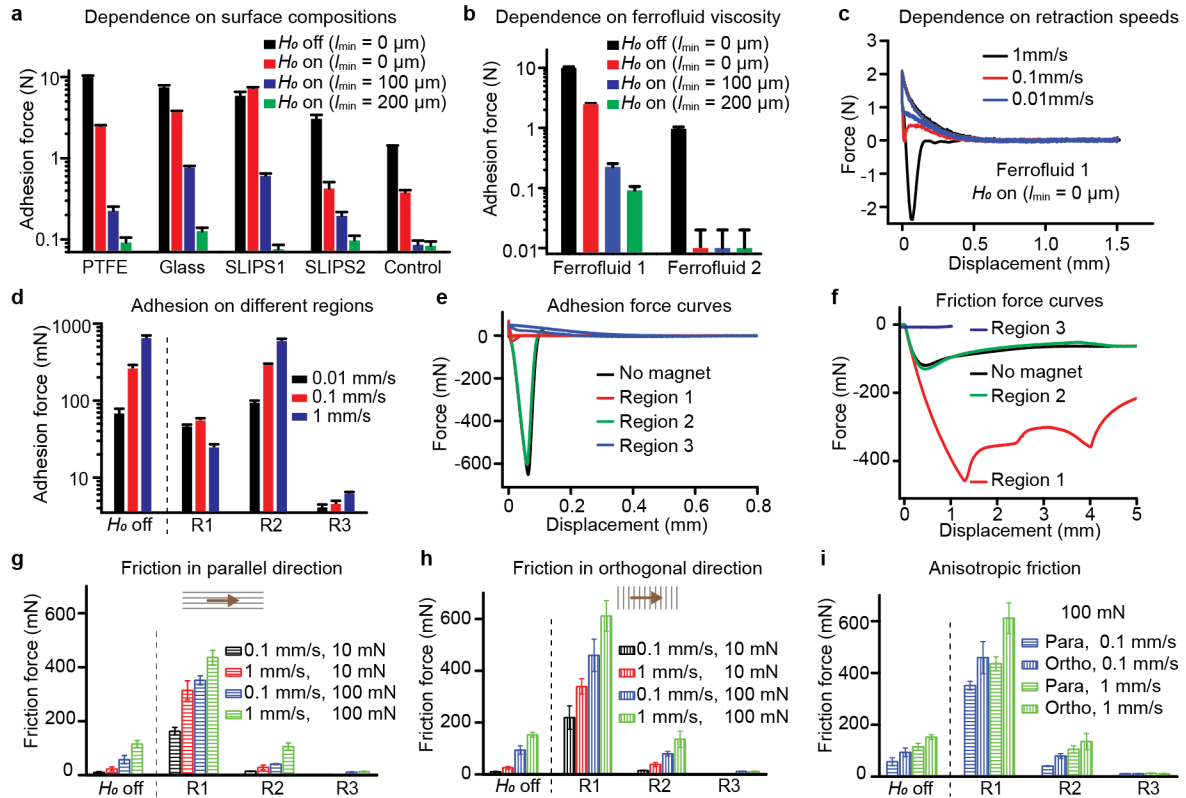
**Extended Data Figure 3. Simulation of magnetic pressure and the fine-tuning of magnetic and capillary pressure balance to create or conceal the micro-topography of FLIPS.** (a) Simulated magnetic field  $B = \mu_0 H_0$  in free space surrounding a  $\frac{1}{2}$ -inch-tall and  $\frac{1}{2}$ -inch-diameter cylindrical neodymium iron boron (NdFeB) magnet. (b) Magnetization curve of ferrofluid 1 (from Ferrotec, Inc). The ferrofluid rapidly reaches its saturation magnetization  $\mu_0 M_s \approx 0.04$  T. The value of saturation magnetization is regarded as a linear function of ferrofluid concentration in the following estimation. (c) Magnetic pressure of ferrofluid 1 in the region above the magnet. The magnetic pressure [kPa] can be considered as the magnetic energy density [kJ/m<sup>3</sup>]. Ferrofluid flows from a high pressure (energy) region to a low pressure (energy) region. (d) Turning on the micro-topographical response.  $|p_m| \sim 10^4$  Pa  $>$   $10^3$  Pa  $\sim p_\gamma$ . (e-g) Turning off the micro-topographical response. (e) Response when the ferrofluid is diluted to 4 % by volume.  $|p_m| \sim 10^2$  Pa  $<$   $10^3$  Pa  $\sim p_\gamma$ . (f) Response using a weaker magnet, Alnico.  $|p_m| \sim 10^3$  Pa  $\sim 10^3$  Pa  $\sim p_\gamma$ . (g) The distance between the repeating units of the microstructure is reduced so that the capillary pressure is increased. The microstructure is Pattern #5, which is a hexagonal array of posts of 1.5  $\mu\text{m}$  in diameter and  $\sim 10$   $\mu\text{m}$  in height. The spacing between posts is 1.4  $\mu\text{m}$ .  $|p_m| \sim 10^4$  Pa  $\sim 10^4$  Pa  $\sim p_\gamma$ . The bottom row of (d-g) shows the corresponding 3D profiles of the ferrofluid-air interface near the magnet. Only in (d) is the interface pulled down towards the bottom of the microstructure.



**Extended Data Figure 4. Wrapping layers around a water droplet in air and in a hydrocarbon on FLIPS and the ability for the macroscopic protuberance to hold a droplet at tilt angles.** (a) Photographs of a water droplet ( $\sim 5 \mu\text{L}$ ) placed on FLIPS with ferrofluid 1 (left) and diluted ferrofluid 1 (right). (b) Photographs of a water droplet ( $\sim 5 \mu\text{L}$ ) placed on FLIPS with ferrofluid 1 (left) and diluted ferrofluid 1 (right) immersed in dodecane. (c) Photographs of a water droplet ( $\sim 5 \mu\text{L}$ ) held by a magnet at  $\sim 90^\circ$  and  $\sim 30^\circ$  on FLIPS with ferrofluid 1 (left) and diluted ferrofluid 1 (right), respectively. (d) Photographs of a water droplet ( $\sim 5 \mu\text{L}$ ) immersed in dodecane and held by a magnet at  $\sim 90^\circ$  and  $\sim 30^\circ$  on FLIPS with ferrofluid 1 (left) and diluted ferrofluid 1 (right), respectively. The comparison between c and d suggests that holding a droplet on the macroscopic protuberance does not require the existence of the wrapping layer and that capillary force is likely to dominate the interaction.



**Extended Data Figure 5. Calculations of the van der Waals interaction energy  $G_{132}$  and disjoining pressure.** (a) Dielectric response  $\epsilon$  as a function of imaginary frequency  $\xi$  for the four phases in the droplet-on-FLIPS system. Note that the ferrofluid line lies between air and water, but below both water and dodecane. (b) Interaction energy as a function of ferrofluid wrapping layer thickness for the water-ferrofluid-dodecane configuration. The energy decreases as the thickness decreases, indicating that the wrapping layer is unstable. (c) Interaction energy as a function of ferrofluid wrapping layer thickness for the water-ferrofluid-air configuration. The energy decreases as the wrapping layer thickness increases, indicating that the wrapping layer is stable. (d) Disjoining pressure as a function of the ferrofluid wrapping layer thickness in the water-ferrofluid-air system. The pressures are positive, indicating the formation of a stable thin film or a stable wrapping layer.



**Extended Data Figure 6. Additional adhesion and friction data.** (a-c) Adhesion measured on FLIPS prepared with isotropic porous Teflon membrane substrates. (a) Adhesion of FLIPS on a low-energy surface (PTFE), a high-energy surface (glass), and two composite surfaces: fluorocarbon oil-based slippery liquid-infused porous surfaces 1 (SLIPS1) and silicone oil-based SLIPS2. The control is measured between two glass surfaces coated with ferrofluid only and without the porous membrane. (b) Dependence of adhesion on ferrofluid viscosity. Ferrofluid 1 ( $\mu = 0.367$  Pa.s) is more viscous than ferrofluid 2 ( $\mu = 0.040$  Pa.s). (c) Dependence of adhesion on retraction speeds. The adhesion decreases with decreasing retraction speeds. The test surface is a PTFE surface. Both b and c suggest that viscous adhesion is the dominant adhesion mechanism. (d-i) Adhesion and friction measurements on FLIPS with anisotropic substrate. Pattern 1 is used. The numbering of regions (R1 – micro-topography, R2 – flat region with a ferrofluid overlayer, R3 – macro-topography) is the same as in Figure 1 in the main text. (d) Adhesion without magnet and on different regions with magnet at three different retraction speeds. (e) Sample adhesion force curves measured at 1 mm/s. (f) Sample friction force curves measured at 1 mm/s and with 100 mN load. The value of the friction force is extracted from the lowest point along the curve. Note a unique signature friction at the micro-topographical area of FLIPS, which is significantly higher than that on either flat or macro-topographical area, characteristic of typical ferrofluid-coated non-structured surfaces. (g) Friction forces without magnets and on different regions with magnet in the direction parallel to the microchannels. Friction is highest in region “1”, in the presence of micro-topography, and lowest in region “3”, in the presence of macro-topography. The friction in region “2”, with a flat fluid overlayer, is the same as for the entire FLIPS surface with no magnetic force. The difference can be as high as two orders of magnitude between regions “1” and “3”, and one order of magnitude between regions “1” and “2” (or between region “1” and with no magnetic force). (h) The corresponding friction forces in orthogonal direction. (i) Direct comparison of friction forces in the parallel and orthogonal directions.

## V. Extended Data Tables

**Extended Data Table 1a. Physical properties of fluorocarbon-based ferrofluids and perfluoropolyether oil (Krytox 100) provided by the manufacturers.**

Name	Density (g/cm <sup>3</sup> )	Dielectric Constant $\epsilon$	Refractive Index $n$	Dynamic Viscosity (Pa·s)	Kinematic Viscosity (cm <sup>2</sup> ·s <sup>-1</sup> )	Volatility	Magnetic Saturation (Gauss)
FC Ferrofluid 1	1.8 - 2.0	2.0*	1.295*	0.367	1.9	0.5% at 100 °C after 3.5h	400
FC Ferrofluid 2	1.7 - 1.9	1.94*	1.28*	0.040	0.22	72.3% at 100 °C after 1.5h	400
Krytox 100	1.87	2.2	1.3	0.013	0.070	87% at 121 °C after 22h	-

Note 1: \* Dielectric constants and refractive indices of pure solvents.

**Extended Data Table 1b. Surface and interfacial tensions of liquids used in the study**

Interfaces	Interfacial Tension (mN/m)	Interfaces	Interfacial Tension (mN/m)
Water – air	73.4±0.2	FF 1 – water	42.9±0.7
Dodecane – air	25.3±0.1	FF 2 – water	37.4±0.6
FF 1 – air	17.1±0.2	4v% FF 1 – water	57.5±0.6
FF 2 – air	13.5±0.1	4v% FF 2 – water	55.3±0.8
4v% FF 1 – air	16.0±0.4	FF 1 – dodecane	6.7±0.2
4v% FF 2 – air	15.6±0.5	FF 2 – dodecane	4.8±0.1
Dodecane – water	44.8±0.1*	4v% FF 1 – dodecane	6.6±0.2
		4v% FF 2 – dodecane	7.1±0.1

Note 2: \*The interfacial tension of a dodecane – water interface is highly sensitive to trace amounts of impurities. Listed value is for dodecane of reagent plus grade from Aldrich. Other measured values include 52.2±0.8 mN/m for analytical standard grade from Aldrich and 45.7±1.0 for 99+% grade from Alpha Aesar.

Note 3: v% represents percentage by volume.

Note 4: Standard deviations are obtained over six or more measurements.

**Extended Data Table 2. Initial spreading coefficients**

<b>Interface 1-2 (<math>\gamma_{12}</math>)</b>	<b>Interface 3-1 (<math>\gamma_{31}</math>)</b>	<b>Interface 3-2 (<math>\gamma_{32}</math>)</b>	<b>Initial Spreading Coefficient <math>S_i = \gamma_{12} - (\gamma_{31} + \gamma_{32})</math> (mN/m)</b>	<b>Agreement with Experiments</b>
Air – water	FF 1 – air	FF 1 – water	13.4	Yes
Air – water	FF 2 – air	FF 2 – water	22.5	Yes
Air – water	4v% FF 1 – air	4v% FF 1 – water	-1.2	No
Air – water	4v% FF 2 – air	4v% FF 2 – water	2.5	Yes
Dodecane – water	FF 1 – dodecane	FF 1 – water	-4.8	Yes
Dodecane – water	FF 2 – dodecane	FF 2 – water	2.6	No
Dodecane – water	4v% FF 1 – dodecane	4v% FF 1 – water	-19.3	Yes
Dodecane – water	4v% FF 2 – dodecane	4v% FF 2 – water	-17.6	Yes

Note:  $S_i > 0$  indicates spreading;  $S_i < 0$  indicates no spreading.

**Extended Data Table 3. The signs of Hamaker constants  $A_{132}$  and van der Waals interaction energy  $G_{132}$  estimated by combining relations**

Medium 1	Medium 3	Medium 2	Hamaker Constant $A_{132}$	van der Waals interaction energy $G_{132}$	Agreement with Experiments
Air	FF 1	Water	<0	>0 (Repulsive)	Yes
Air	FF 2	Water	<0	>0 (Repulsive)	Yes
Air	4v% FF 1	Water	<0	>0 (Repulsive)	Yes
Air	4v% FF 2	Water	<0	>0 (Repulsive)	Yes
Dodecane	FF 1	Water	>0	<0 (Attractive)	Yes
Dodecane	FF 2	Water	>0	<0 (Attractive)	Yes
Dodecane	4v% FF 1	Water	>0	<0 (Attractive)	Yes
Dodecane	4v% FF 1	Water	>0	<0 (Attractive)	Yes

Note: Only the sign of the vdW interaction energy is needed to predict the formation or the absence of the wrapping layer.

**Extended Data Table 4. Nonretarded Hamaker constants  $A_{132}$  and van der Waals interaction energy  $G_{132}$  based on Lifshitz theory**

Medium 1 – 3 – 2	$A_{v=0}$ (J)	$A_{v>0}$ (J)	$A_{Total}$ (J)	van der Waals interaction energy $G_{132}$	Agreement with Experiments
Air – FF1 – Water	$-9.8 \times 10^{-22}$	$-3.1 \times 10^{-21}$	$-4.1 \times 10^{-21}$	>0 (Repulsive)	Yes
Air – FF2 – Water	$-9.4 \times 10^{-22}$	$-4.2 \times 10^{-21}$	$-5.1 \times 10^{-21}$	>0 (Repulsive)	Yes
Air – 4v% FF1 – Water	$-1.1 \times 10^{-21}$	$-2.7 \times 10^{-21}$	$-3.8 \times 10^{-21}$	>0 (Repulsive)	Yes
Air – 4v% FF2 – Water	$-1.1 \times 10^{-21}$	$-2.7 \times 10^{-21}$	$-3.8 \times 10^{-21}$	>0 (Repulsive)	Yes
Dodecane – FF1 – Water	$7.3 \times 10^{-24}$	$1.2 \times 10^{-21}$	$1.2 \times 10^{-21}$	<0 (Attractive)	Yes
Dodecane – FF2 – Water	$5.2 \times 10^{-23}$	$1.8 \times 10^{-21}$	$1.9 \times 10^{-21}$	<0 (Attractive)	Yes
Dodecane – 4v% FF1 – Water	$-1.3 \times 10^{-22}$	$9.6 \times 10^{-22}$	$8.3 \times 10^{-22}$	<0 (Attractive)	Yes

## **VI. Description of supplementary videos**

### **Video 1** FLIPS dual level topographical response

This video first shows the top view of FLIPS' topographical responses, particularly the expansion of the micro-topographical area over time. The second and the third parts of the video show FLIPS' topographical response to a hexagon of six magnets and arrays of magnets with hexagonal symmetries, respectively.

### **Video 2** Transport of colloidal particles

This video shows the controlled transport of non-magnetic colloidal particles on FLIPS. A magnetic field gradient is applied and removed repeatedly in the direction of the colloids' movement through the usage of a small permanent magnet.

### **Video 3** Switching droplet mobility by removing micro-topography

This video shows that a droplet is first pinned on the micro-topographical area. Once the magnet is lowered to switch the balance between magnetic pressure and capillary pressure, ferrofluid flows back to the micro-topographical area, allowing the droplet to slide again. The second part of the video is taken using a smaller FLIPS and a smaller magnet, and under angled illumination.

### **Video 4** Assembling droplets by fine-tuning the macro-topographical response.

This video shows that droplets are assembled *via* the macroscopic protuberance and released in clusters of two to five.

### **Video 5** Wrapping and unwrapping of a ferrofluid layer around a water droplet

This video first shows the spontaneous formation of a layer of ferrofluid around a water droplet and its thinning under a magnetic field. When dodecane is added to replace air, the wrapping layer is removed.

### **Video 6** Mixing with and without the ferrofluid wrapping layer

This video first demonstrates that the presence of the wrapping layer delays mixing. Two droplets of polystyrene colloids are brought together, but mixing occurs only after the wrapping layer is disrupted by the pulses of the electromagnet. The second half of the video shows instantaneous mixing when wrapping layers are absent.

### **Video 7** Switchable adhesion

In this video, FLIPS creates strong adhesion between a top handle and a bottom frame in which a beaker of water sits without magnets. After magnets are installed, the adhesion is reduced, and it is able to separate the top handle from the bottom frame. Removing magnets switches FLIPS back to its adhesive state.

### **Video 8** Switchable friction

In this video, the top central cylindrical disk has FLIPS attached to its bottom, and its rotation is due to the friction between the FLIPS and a stage connected to a step motor. After magnets are

installed, the friction is reduced, and the rotation stops. Removing magnets allows the rotation to resume.

### **Video 9 Pumping**

This video demonstrates the pumping capability of a FLIPS pipe. It shows an ethanol solution of Rhodamine B being pumped from the right glass vial to the left glass vial, followed by an explanatory animation.

### **Video 10 Biofilm removal**

This video shows that the topographical responses of FLIPS disrupt and detach an algae biofilm from the FLIPS substrate.

## **VII. Supplementary references**

- 1 Pokroy, B., Epstein, A. K., Persson-Gulda, M. C. M. & Aizenberg, J. Fabrication of bioinspired actuated nanostructures with arbitrary geometry and stiffness. *Adv. Mater.* **21**, 463 (2009).
- 2 Kim, P., Adorno-Martinez, W. E., Khan, M. & Aizenberg, J. Enriching libraries of high-aspect-ratio micro- or nanostructures by rapid, low-cost, benchtop nanofabrication. *Nature Protocols* **7**, 311 (2012).
- 3 Acheson, D. J. *Elementary Fluid Dynamics*. (Oxford University Press Inc., New York, 1990).
- 4 de Gennes, P.-G., Brochard-Wyart, F. & Quéré, D. *Capillarity and Wetting Phenomena : Drops, Bubbles, Pearls, Waves*. (Springer, 2004).
- 5 Hardy, W. B. The tension of composite fluid surfaces and the mechanical stability of films of fluid. *P R Soc Lond A-Conta* **86**, 610-635 (1912).
- 6 Hardy, W. B. The Tension of Composite Fluid Surfaces. No. II. *P R Soc Lond A-Conta* **88**, 313-333 (1913).
- 7 Smith, J. D. *et al.* Droplet mobility on lubricant-impregnated surfaces. *Soft Matter* **9**, 1772-1780 (2013).
- 8 Schellenberger, F. *et al.* Direct observation of drops on slippery lubricant-infused surfaces. *Soft Matter* **11**, 7617-7626 (2015).
- 9 Bonn, D., Eggers, J., Indekeu, J., Meunier, J. & Rolley, E. Wetting and spreading. *Rev Mod Phys* **81**, 739-805 (2009).
- 10 Parsegian, V. A. *Van der Waals Forces : a Handbook for Biologists, Chemists, Engineers, and Physicists*. (Cambridge University Press, 2006).
- 11 Israelachvili, J. N. *Intermolecular and Surface Forces*. 3rd edn, (Academic Press, 2011).
- 12 Reiter, G. *et al.* Thin film instability induced by long-range forces. *Langmuir* **15**, 2551-2558 (1999).
- 13 Fowkes, F. M. Attractive forces at interfaces. *Ind Eng Chem* **56**, 40-52 (1964).